Prepared in cooperation with the Ministry of Petroleum, Energy and Mines, Islamic Republic of Mauritania

Second Projet de Renforcement Institutionnel du Secteur Minier de la République Islamique de Mauritanie (PRISM-II)

Synthesis of Geophysical Data:

Phase V, Deliverable 55

By Carol A. Finn and Eric D. Anderson

Open-File Report 2013–1280 Chapter B

U.S. Department of the Interior
U.S. Geological Survey

U.S. Department of the Interior
SALLY JEWELL, Secretary

U.S. Geological Survey
Suzette M. Kimball, Acting Director

U.S. Geological Survey, Reston, Virginia: 2015

Suggested citation:
Finn, C.A., and Anderson, E.D., 2015, Synthesis of geophysical data (phase V, deliverable 55), chap. B *of* Taylor, C.D., ed., Second projet de renforcement institutionnel du secteur minier de la République Islamique de Mauritanie (PRISM-II): U.S. Geological Survey Open-File Report 2013–1280-B, 60 p., http://dx.doi.org/10.3133/ofr20131280. [In English and French.]

Multiple spellings are used in various literatures, and may be reflected in the text.

This report is preliminary and has not been reviewed for conformity with U.S. Geological Survey editorial standards or for stratigraphic nomenclature.

The report is being released in both English and French. In both versions, we use the French-language names for formal stratigraphic units.

ISSN 2331-1258 (online)

Synthesis of Geophysical Data

Summary

Aeromagnetic and radiometric data were used to map shallow Precambrian basement lithology and structure and determine the depth to magnetic basement, which in most cases, corresponds to the depth to crystalline basement of interest for mineral exploration. These depths, along with those determined from gravity data, help identify basins with hydrologic potential. In addition, the magnetic data were used to identify buried Precambrian rocks of unknown affinity.

Contents

Figures

Tables

Conversion Factors

SI to Inch/Pound

Multiply	By	To obtain
	Length	
centimeter (cm)	0.3937	inch (in.)
millimeter (mm)	0.03937	inch (in.)
decimeter (dm)	0.32808	foot (ft)
meter (m)	3.281	foot (ft)
kilometer (km)	0.6214	mile (mi)
	Area	
hectare (ha)	2.471	Acre
square meter (m^2)	0.0002471	acre
square kilometer (km^2)	0.3861	square mile (mi^2)
	Volume	
cubic kilometer (km^3)	0.2399	cubic mile (mi^3)
	Mass	
gram (g)	0.03527	ounce, avoirdupois (oz)
kilogram (kg)	2.205	pound avoirdupois (lb)
megagram (Mg)	1.102	ton, short (2,000 lb)
megagram (Mg)	0.9842	ton, long (2,240 lb)
metric ton per day	1.102	ton per day (ton/d)
megagram per day (Mg/d)	1.102	ton per day (ton/d)
metric ton per year	1.102	ton per year (ton/yr)
	Pressure	
kilopascal (kPa)	0.009869	atmosphere, standard (atm)
kilopascal (kPa)	0.01	Bar
	Energy	
joule (J)	0.0000002	kilowatt hour (kWh)

ppm, parts per million; ppb, parts per billion; Ma, millions of years before present; m.y., millions of years; Ga, billions of years before present; 1 micron or micrometer (µor µm) = 1×10^{-6} meters; Tesla (T) = the field intensity generating 1 Newton of force per ampere (A) of current per meter of conductor

Temperature in degrees Celsius (°C) may be converted to degrees Fahrenheit (°F) as follows:

°F=(1.8×°C)+32

Temperature in degrees Fahrenheit (°F) may be converted to degrees Celsius (°C) as follows:

°C=(°F-32)/1.8

Coordinate information is referenced to the World Geodetic System (WGS 84)

Acronyms

AMT	Audio-magnetotelluric
ASTER	Advanced Spaceborne Thermal Emission and Reflection Radiometer
AVIRIS	Airborne Visible/Infrared Imaging Spectrometer
BIF	Banded iron formation
BLEG	Bulk leach extractable gold
BGS	British Geological Survey
BRGM	Bureau de Recherches Géologiques et Minières (Islamic Republic of Mauritania)
BUMIFOM	The Bureau Minier de la France d'Outre-Mer
CAMP	Central Atlantic Magmatic Province
CGIAR-CSI	Consultative Group on International Agricultural Research-Consortium for Spatial information
DEM	Digital Elevation Model
DMG	Direction des Mines et de la Géologie
EC	Electrical conductivity
EMPA	Electron Microprobe Analysis
EM	Electromagnetic (geophysical survey)
EOS	Earth Observing System
eU	Equivalent uranium
GGISA	General Gold International
GIF	Granular iron formation
GIFOV	Ground instantaneous field of view
GIS	Geographic Information System
HIF	High grade hematitic iron ores
IHS	Intensity/Hue/Saturation
IAEA	International Atomic Energy Agency
IOCG	Iron oxide copper-gold deposit
IP	Induced polarization (geophysical survey)
IRM	Islamic Republic of MauritaniaIslamic Republic of Mauritania
JICA	Japan International Cooperation Agency
JORC	Joint Ore Reserves Committee (Australasian)
LIP	Large Igneous Province
LOR	Lower limit of reporting
LREE	Light rare-earth element
METI	Ministry of Economy, Trade and Industry (Japan)
MICUMA	Société des Mines de Cuivre de Mauritanie
MORB	Mid-ocean ridge basalt
E-MORB	Enriched mid-ocean ridge basalt
N-MORB	Slightly enriched mid-ocean ridge basalt
T-MORB	Transitional mid-ocean ridge basalt

Moz	Million ounces
MVT	Mississippi Valley-type deposits
NASA	United States National Aeronautics and Space Administration
NLAPS	National Landsat Archive Processing System
OMRG	Islamic Republic of Mauritanian Office for Geological Research
ONUDI	(UNIDO) United Nations Industrial Development Organization
PRISM	Projet de Renforcement Institutionnel du Secteur Minier
PGE	Platinum-group elements
RC	Reverse circulation drilling
REE	Rare earth element
RGB	Red-green-blue color schema
RTP	Reduced-to-pole
SARL	Société à responsabilité limitée
SEDEX	Sedimentary exhalative deposits
SIMS	Secondary Ionization Mass Spectrometry
SNIM	Société National Industrielle et Minière (Islamic Republic of Mauritania)
SP	Self potential (geophysical survey)
SRTM	Shuttle Radar Topography Mission
SWIR	Shortwave infrared
TDS	Total dissolved solids
TIMS	Thermal Ionization Mass Spectrometry
TISZ	Tacarat-Inemmaudene Shear Zone
TM	Landsat Thematic Mapper
UN	United Nations
UNDP	United Nations Development Program
US	United States
USA	United States of America
USGS	United States Geological Survey
UTM	Universal Transverse Mercator projection
VHMS	Volcanic-hosted massive sulfide
VisNIR	Visible near-infrared spectroscopy
VLF	Very low frequency (geophysical survey)
VMS	Volcanogenic massive sulfide deposit
WDS	Wavelength-dispersive spectroscopy
WGS	World Geodetic System

Second Projet de Renforcement Institutionnel du Secteur Minier de la République Islamique de Mauritanie (PRISM-II)

Synthesis of Geophysical Data: Phase V, Deliverable 55

By Carol A. Finn[1] and Eric D. Anderson[1]

1 Introduction

Aeromagnetic data provide a means for seeing through surficial layers such as sand, vegetation, and water, and are a powerful tool for delineating crystalline basement beneath cover rocks and estimating depths to magnetic sources. Airborne gamma-ray data provide estimates of the potassium, uranium, and thorium concentrations in rocks and soils at the ground surface. Because these radioactive elements are lithophile elements, their distributions reflect lithologic differences and therefore can be used as an aid to geologic mapping. Where faults have resulted in significant offset either vertically or horizontally, linear patterns in the data may be observable. Geochemical processes also affect the distribution of the radioactive elements and patterns observed in the data can be used to identify areas where such processes may have been active.

The primary goals of the geophysics component of this project is to construct a geologic basement map relevant to mineral and water exploration and add to the structural map by adding buried features identified in the magnetic data. To this end, several analysis tools are applied to the datasets to enhance features of interest as well as to estimate depths to magnetic sources. Figures are embedded in the text. Four 1:1M scale separate maps are associated with this report (Finn and Horton, 2015).

2 Aeromagnetic Data

Magnetic anomalies reflect variations in the distribution and type of magnetic iron oxide minerals—primarily magnetite—in Earth's crust. Aeromagnetic data generally image the upper ~10 km of crust and extend geological mapping of exposed crystalline basement into covered areas. Horizontal resolution depends on flight line spacing and height of survey, but ranges from meters to continental scales. At regional scales, magnetic highs are often associated with magnetite-rich batholiths, large volumes of volcanic rocks and metamorphic rocks with mafic igneous protoliths. At regional scales, magnetic lows (blue colors on magnetic maps) can be caused by magnetite-poor sedimentary rocks, reversely magnetized or altered volcanic rocks,

[1]U.S. Geological Survey, Denver Federal Center, Denver, Colorado 80225 U.S.A.

felsic plutons and metamorphic rocks with sedimentary protoliths. At local scales, magnetic highs relate to normally magnetized dikes, edges of sills, banded iron formations (BIFs), ophiolites, and Jurassic volcanic flows; magnetic lows correspond to greenstone belts, altered igneous rocks, and reversely magnetized dikes and volcanic rocks.

Aeromagnetic data were collected by FUGRO and Sanders during the PRISM-I project at a flight height of about 100 m above terrain with line spacing of 500 m in the north and 700 m elsewhere in 1 degree blocks. Tie lines were flown perpendicular to flight lines spaced 10 times the flight line spacing for all surveys. The lines were flown north-south in the Northwestern, Southern regions and east-west in the western and northern zones (fig. 1). All data were merged and gridded at a spacing of 175 m (fig. 1). In addition, high resolution data, flown a height of ~100 m in northwest trending lines spaced 250 m over Tasiast and Tijirit, north trending lines spaced 250 m over Inchiri and 400 m spaced east west lines over South Tasiast (fig. 1) were gridded at a spacing of 75 m and used in the mineral assessments. We obtained gridded magnetic and radiometric data from older surveys contracted by the United Nations (U.N.) (Numbered blocks, fig. 1) to augment the new data supplied as part of this contract. The flight line spacing and flight height for the U.N. data are unknown. The grid spacing of the datasets ranged from 1–5 km, which would typically reflect flight line spacing of 200–1,000 m, but this cannot be confirmed. As radiometric data, which cannot be flown higher than ~100 m, were flown with the magnetic data, we estimate that the maximum survey flight height is ~100 m, the same as for the newer data. Both the new and U.N. datasets were regridded to 500 m and merged together assuming the 100 m flight elevation (fig. 1). The interpretation of the merged datasets must be handled with care as the different line spacing within the U.N. data and in comparison to the new data can alias anomalies.

Additional data were flown by Sander over the northern Taoudeni basin in 2008 along north-south lines spaced 500 m apart at an average elevation of ~100 m. These data were gridded at a spacing of 175 m, merged with the existing data and were used to facilitate interpretation on separate map sheets (Finn and Horton, 2015). Further data processing was not done as this was beyond the scope of the contract and is not discussed here.

The geologic interpretation of the magnetic data is aided by filtering the data in a variety of ways and by determining the depth to magnetic sources. In the following sections we discuss the various filters that we used to enhance particular aspects of the data so that we could generate a geologic basement map that includes structures such as faults and dikes. Interpretations were constrained in part by magnetic susceptibility measurements that were made at outcrop and on samples in the lab using a hand held magnetic susceptibility meter. These measurements are included in appendix 1.

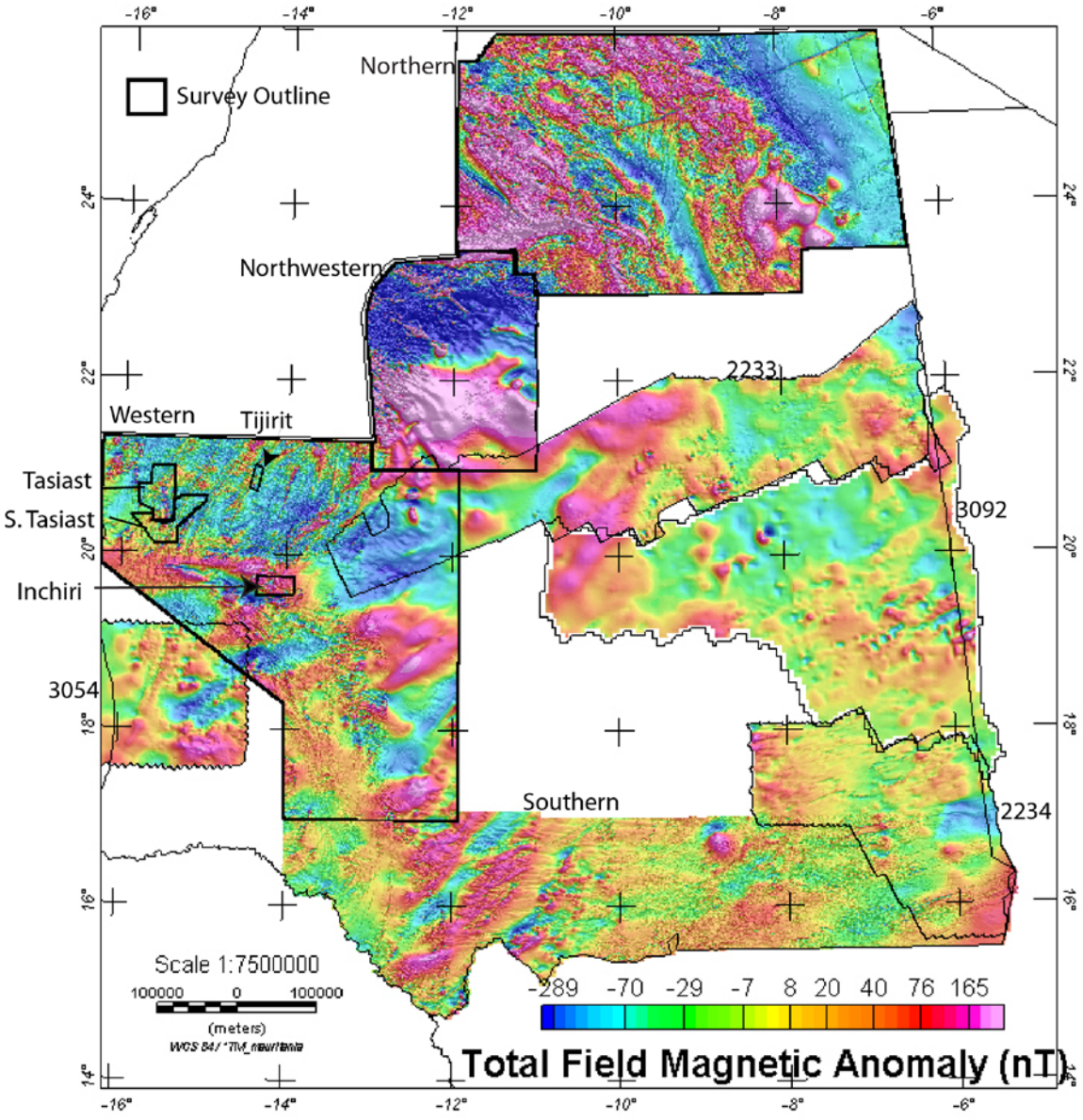

Figure 1. Color-shaded relief image of the total field magnetic anomaly.

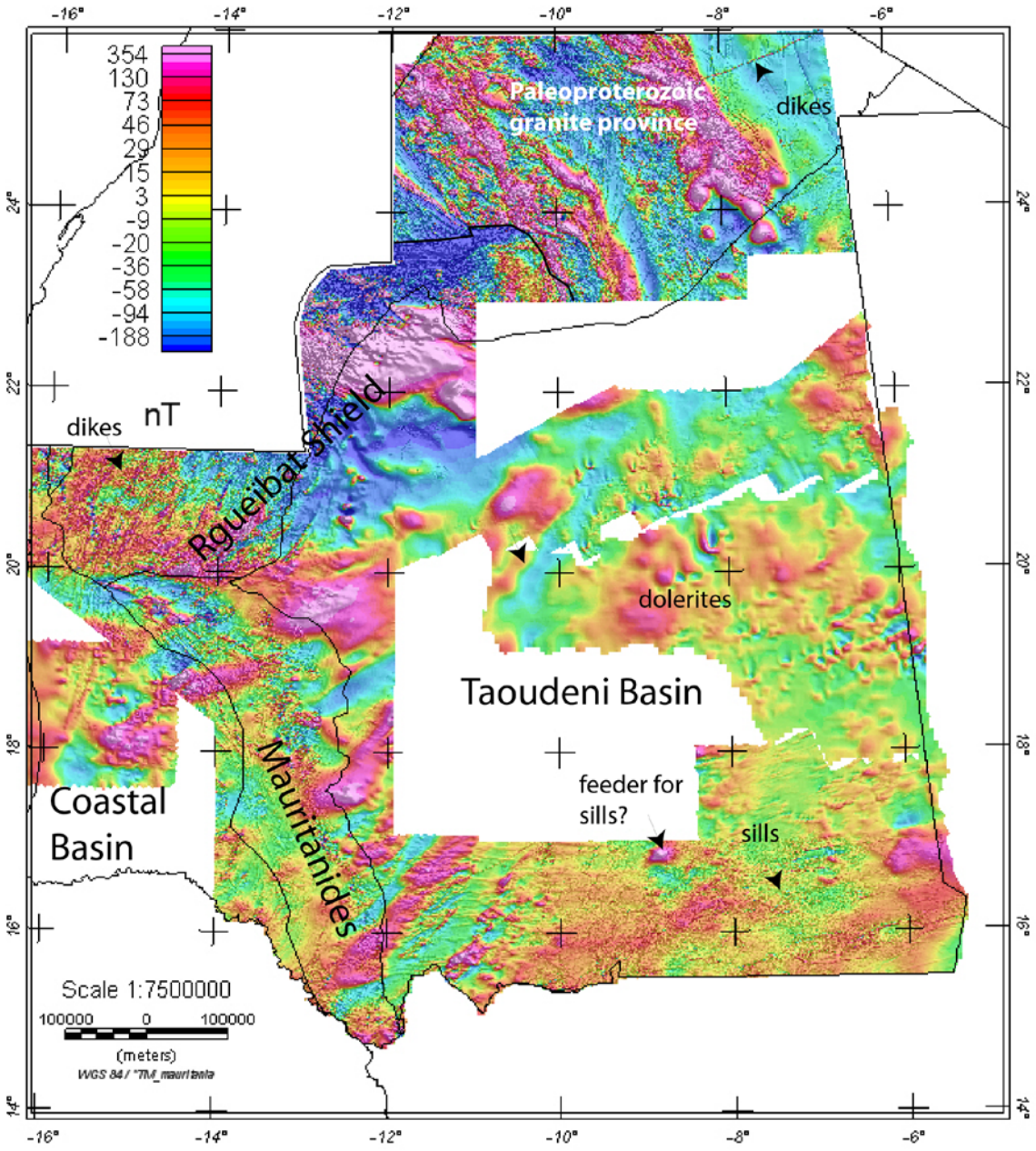

Figure 2. Color-shaded relief image of reduced to the pole total field magnetic anomalies.

2.1 Filtering Tests

To facilitate geologic interpretation, several filtering techniques were applied to the magnetic data. These filters were applied using Oasis Montaj and public USGS software (Phillips, 1997). The magnetic data were filtered (reduced to the pole, RTP) to move anomalies over their sources, define the trend and boundaries of structures and separate anomalies with varying frequencies. Various parameters were applied in the reduction to the pole filter (figs. 1 and 2). Application of the pseudogravity transform (fig. 3) highlights regional anomalies and

simplifies magnetic contact detection analysis. Several common techniques were used to accentuate high frequency anomalies associated with shallow sources. These included upward continuing the RTP magnetic data (figs. 1 and 2) a small interval to generate a regional field (for example, calculating the magnetic field as if it was measured above the actual measurement surface) and then subtracting this regional field from the unfiltered dataset, high-frequency-passed filtering and match filtering. Match filters (figs. 4 and 5) were applied to separate shallow (fig. 6) from deep magnetic sources (fig. 7). Filtering techniques such as analytic signal, maximum horizontal gradient (fig. 9) and terracing (fig. 31) were applied to define magnetic contacts. For the 1:1,000,000 scale of the products, the optimum method was the maximum horizontal gradient of the pseudogravity (fig. 9). Shaded-relief images also highlight the trend of geologic sources (figs. 1 and 2).

2.2 Data Processing

The optimal filters were applied to the entire national magnetic database. These methods were combined to generate a depth to crystalline basement map (fig. 11; Finn and Horton, 2015)) and inferred crystalline basement map (fig. 17).

2.2.1 Reduction to the Pole

The first step is to reduce the observed magnetic data to the pole, a technique designed to account for the inclination of the Earth's magnetic field (figs. 1 and 2). Its principal effect is to shift magnetic anomalies to positions directly above their sources (Baranov and Naudy, 1964; Blakely, 1995). The correction accounts for the effects of inclination and declination, assuming that the total magnetization vectors of the various anomaly sources are within about 25 degrees of being collinear with the Earth's field (induced, not remnant magnetization) (Bath, 1968). This assumption holds true for many of the rocks in the region as the dominant magnetizations for the plutonic and metamorphic rocks in the region are induced. Exceptions are rare reversely magnetized dikes. Reduction to the pole works best if the magnetic sources are vertically dipping. This assumption is probably reasonable for the banded iron formations, dikes and edges of sills that comprise most magnetic sources in the region, but will not hold as well for plutons.

At the low magnetic latitudes of the Islamic Republic of Mauritania (~22^o), the inclination of the magnetic field is shallow, meaning that a normally magnetized body produces a magnetic low instead of a high as at higher magnetic latitudes. The reduction to the pole transformation converts negative anomalies to positive. Also, the amplitude correction for north-south features, particularly those parallel to the declination direction, amplifies noise and distorts the shapes of magnetic anomalies from sources magnetized in directions different from the inducing field (Hansen and Pawlowski, 1989). Instead of assigning a standard amplitude correction of 20^o, we used 90^o, which is equivalent to not filtering the magnetic data. Although high frequency noise along the lines of declination is observed, anomaly shape is maintained as compared with the observed data and correlation with geologic units such as BIFs and dikes.

2.2.2 Pseudogravity

Another filter routinely applied to magnetic data coverts magnetic total-field anomalies to pseudogravity (magnetic potential) anomalies. This has been historically known as the

pseudogravity transform, because the resulting pseudogravity anomaly has the mathematical form of a gravity anomaly (Baranov and Naudy, 1964; Blakely, 1995). As with reduced to pole anomalies, pseudogravity anomalies are centered over their sources to the extent that the magnetic vector assumed is correct. Pseudogravity anomalies are useful for geologic interpretation because longer wavelength anomalies and their thick, broad sources are accentuated at the expense of higher frequency anomalies and their shallow, narrow sources (fig. 3). This transform allows interpretation of regional scale magnetic sources, comparison with gravity anomalies and can aid in the interpretation of tectonic history.

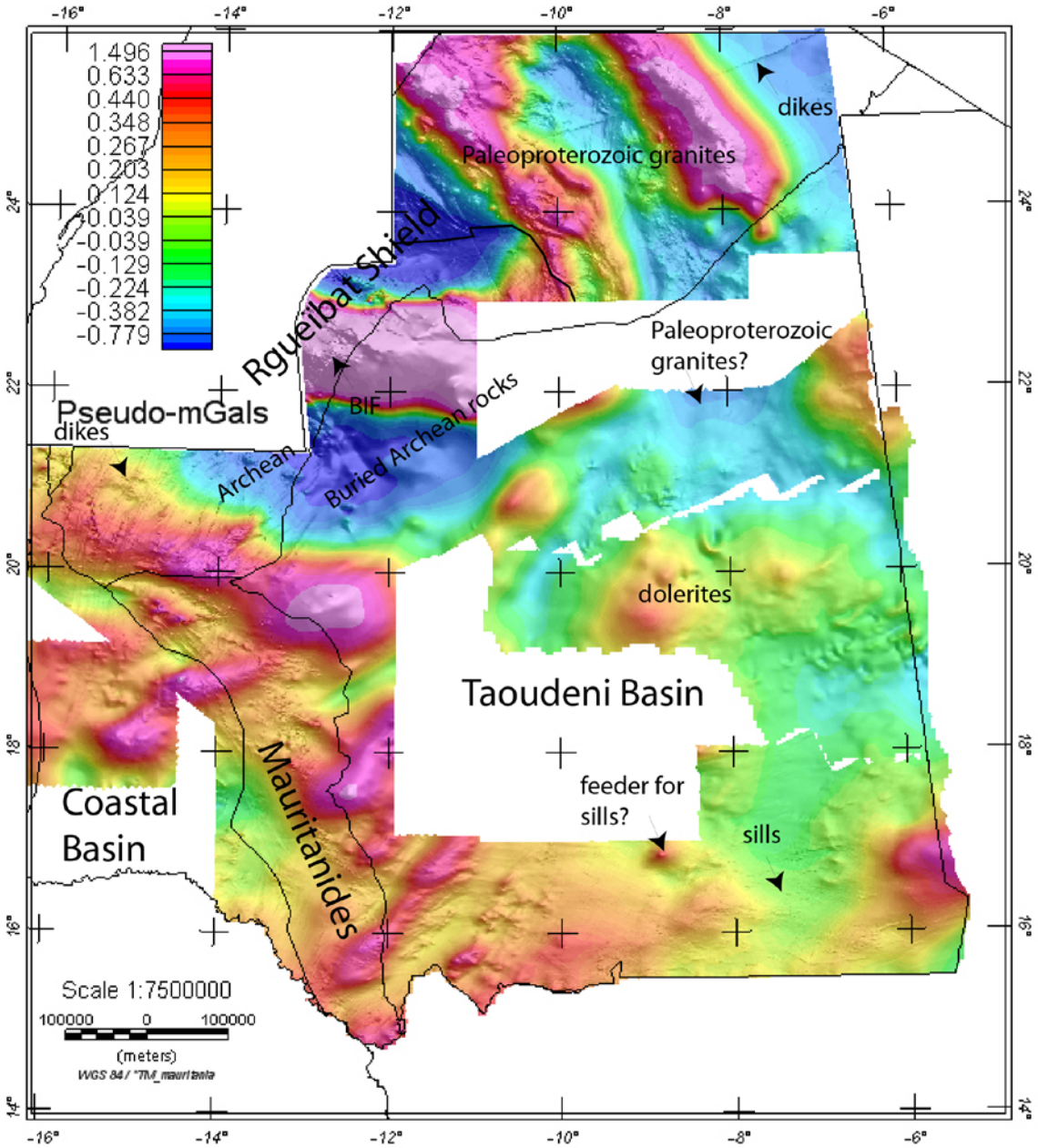

Figure 3. Color-shaded relief image of the pseudogravity of the total field magnetic data.

2.2.2 Match Filtering

Matched bandpass filtering separates potential-field data into anomaly components representing different source depths (Phillips, 2001). The implementation of the filtering was applied to the Islamic Republic of Mauritania magnetic data (fig. 2) using a GX in Oasis Montaj based on a USGS software package (Phillips, 1997). Matched filtering is accomplished in three steps. The initialization program first prepares the input data grid for Fourier transform by extending the rows and columns and then computes the Fourier transform and the natural logarithms of the radially-symmetric part (RSP) of the Fourier power spectrum and the non-radially symmetric part of the power spectrum. The matched bandpass filters are designed interactively by fitting equivalent source layers to the log of RSP power (fig. 4) and also non-linearly adjusts the equivalent layer parameters to better fit the observed spectrum. The actual bandpass filtering (fig. 5) calculates the inverse Fourier transforms and removes the row and column extensions (Phillips, 2001).

The RSP of the power spectrum of the Islamic Republic of Mauritania data was matched by a three-layer equivalent model (fig. 4), consisting of two shallow equivalent dipole layers and a single deep equivalent magnetic half space. The three corresponding bandpass filters (fig. 5) were applied to the new data (fig. 1) and data merged with the U.N. (fig. 2).

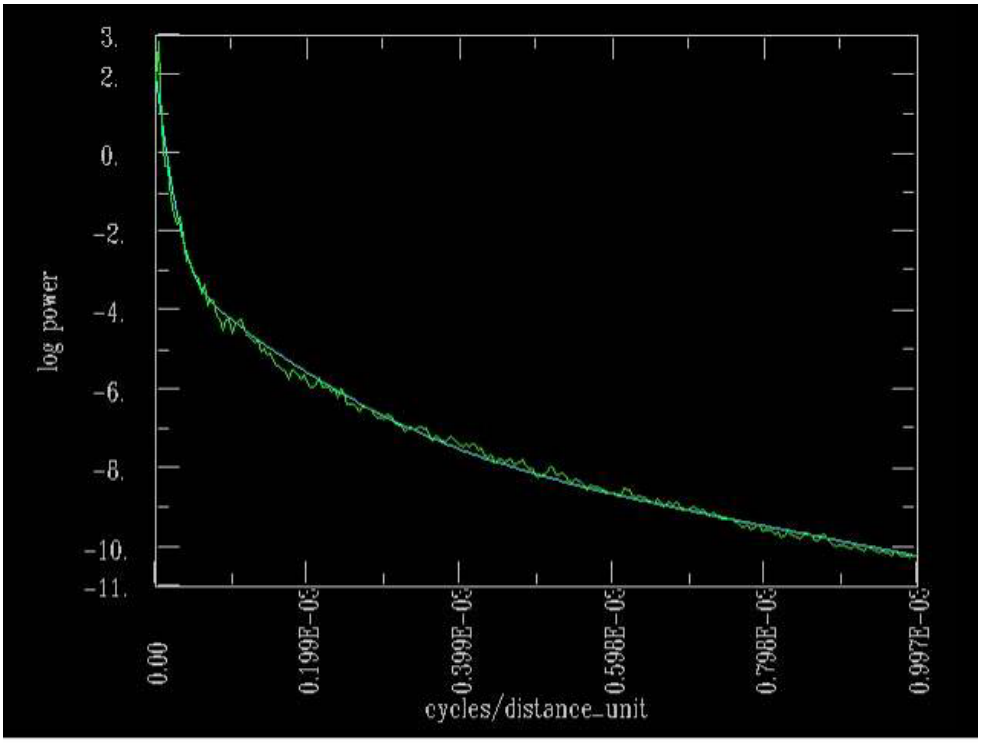

Figure 4. The radially symmetric power spectrum of the data (green) and the power spectrum of a matching three-layer equivalent model (smooth blue line).

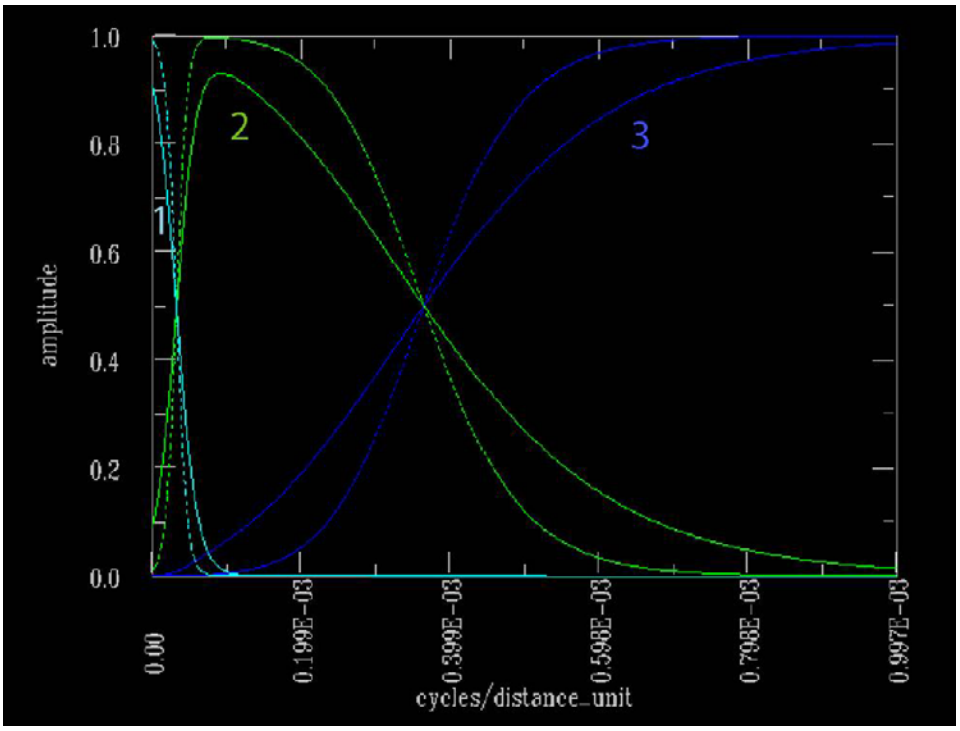

Figure 5. The matched bandpass filters corresponding to the three equivalent layers.

The results of applying bandpass filters 1 and 2 to the data are shown in Figures 6 and 7 respectively. Bandpass 3 (not shown) was not used in the analysis because it primarily contained very short-wavelength, low-amplitude noise and small anomalies associated with dikes, sills and banded iron formation (BIFs) that are contained in the bandpass 2 filtered data. In the Islamic Republic of Mauritania, matched bandpass filtering was used to separate the anomalies produced by the shallow dikes, sills, BIFs and ophilolites (fig. 6) from anomalies produced by deeper crystalline basement (fig. 7). This low frequency magnetic map looks similar to the pseudo gravity map (fig. 3).

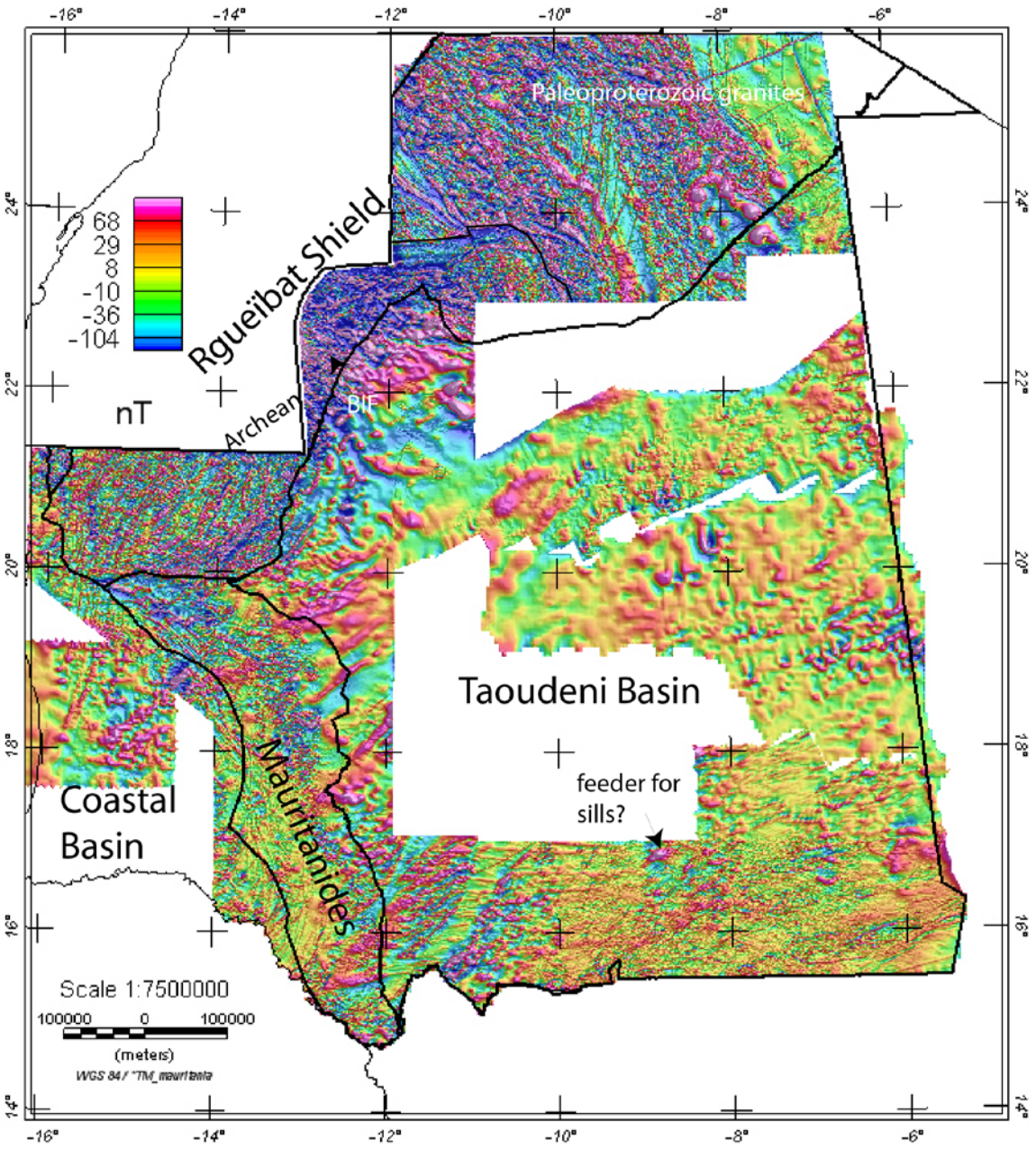

Figure 6. Bandpass filtered image (filter 2, fig. 5) of the magnetic data.

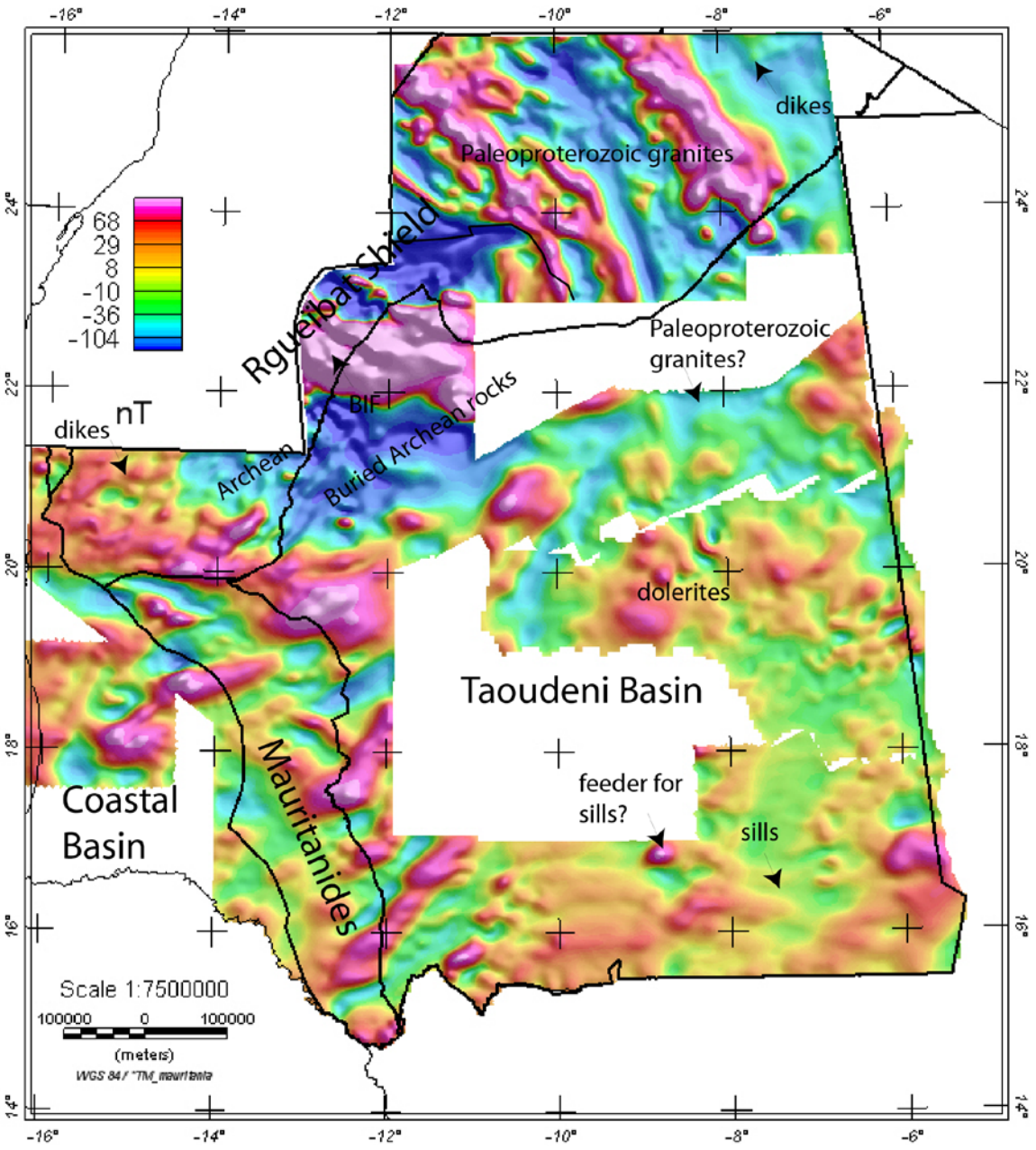

Figure 7. Bandpass filtered image (filter 1, fig. 5) of the magnetic data.

2.2.3 Upward Continuation and Subtraction from RTP Data

Upward continuation transforms the magnetic field (here the reduced to the pole field) measured at one surface (in this case, 100 m above the ground) to the field that would be measured on another surface farther from the sources (here, 200 m above the ground). This transformation attenuates anomalies with respect to wavelength, the shorter the wavelength, the greater the attenuation (Blakely, 1995). A common technique to sharpen the effects of near-

surface sources is to upward continue the magnetic data a small interval to generate a regional field and then subtract this regional field from the unfiltered dataset (the observed reduced to the pole map) to derive a residual or high-frequency-passed magnetic field associated with shallow sources. The resulting filtered map (fig. 8) of the new data is essentially a structure map (Finn and Horton, 2015)—highlighting fracture patterns within granites, dikes, BIFs, tectonic "fabric" within the Mauritanides, edges of sills, etc.

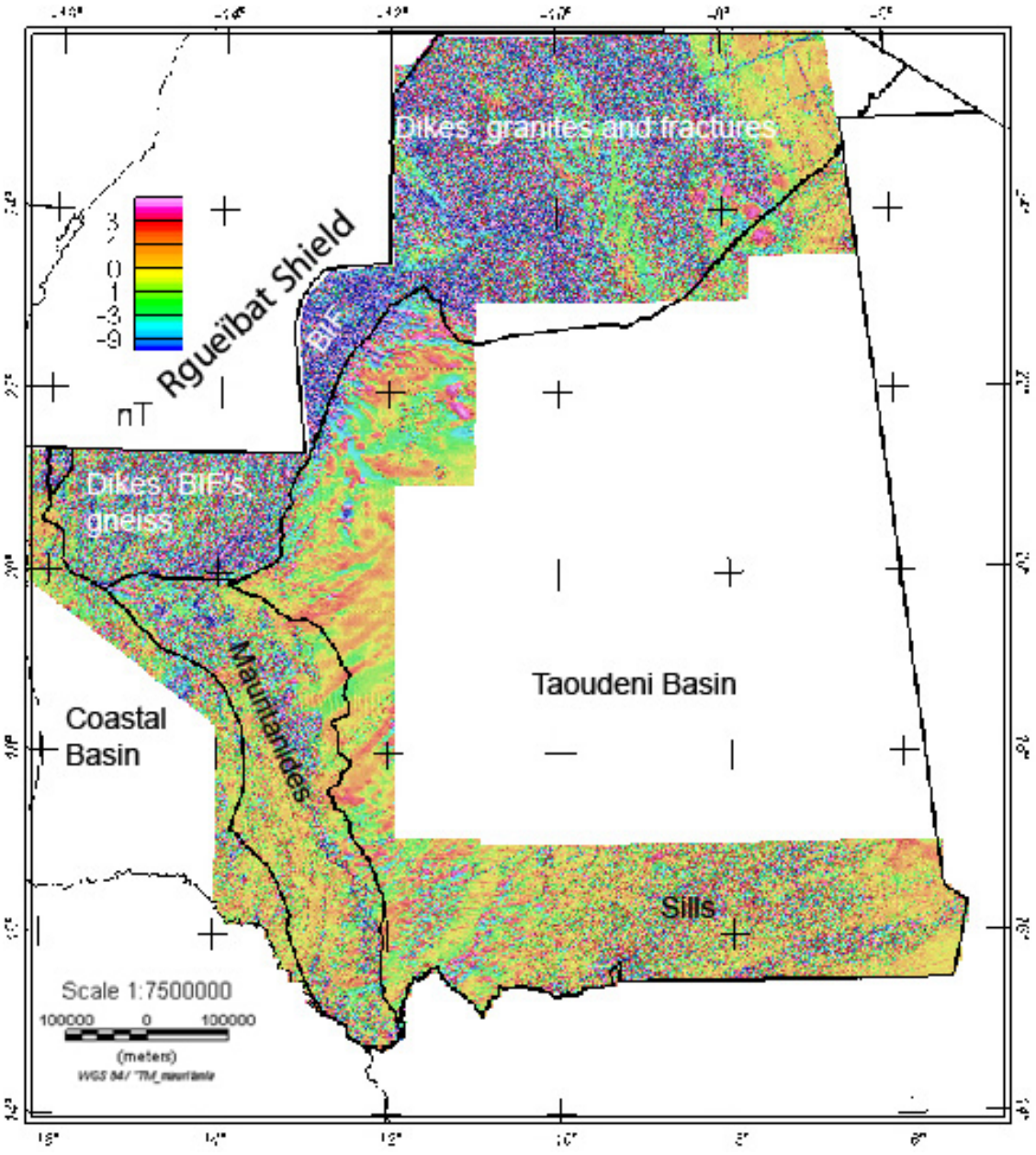

Figure 8. Residual map derived from subtracting the upward continued (by 100 m) reduced to pole magnetic data from the original reduced to pole (fig. 1) data.

2.2.4 Maximum Horizontal Gradient

In order to identify magnetic contacts that might represent faults, fractures or lithologic boundaries, a function is applied to the aeromagnetic data, called the maximum horizontal gradient that is peaked over the contacts (Blakely and Simpson, 1986; Cordell and Grauch, 1985; Grauch and Cordell, 1987). Transforming the magnetic data into the pseudogravity simplifies the interpretation of magnetic anomalies because the horizontal gradient peaks of pseudogravity anomalies are centered directly over vertical contacts separating rocks with different magnetizations, just as the horizontal gradients of gravity anomalies lie over vertical contacts separating rocks of differing density (Blakely and Simpson, 1986; Cordell and Grauch, 1985).

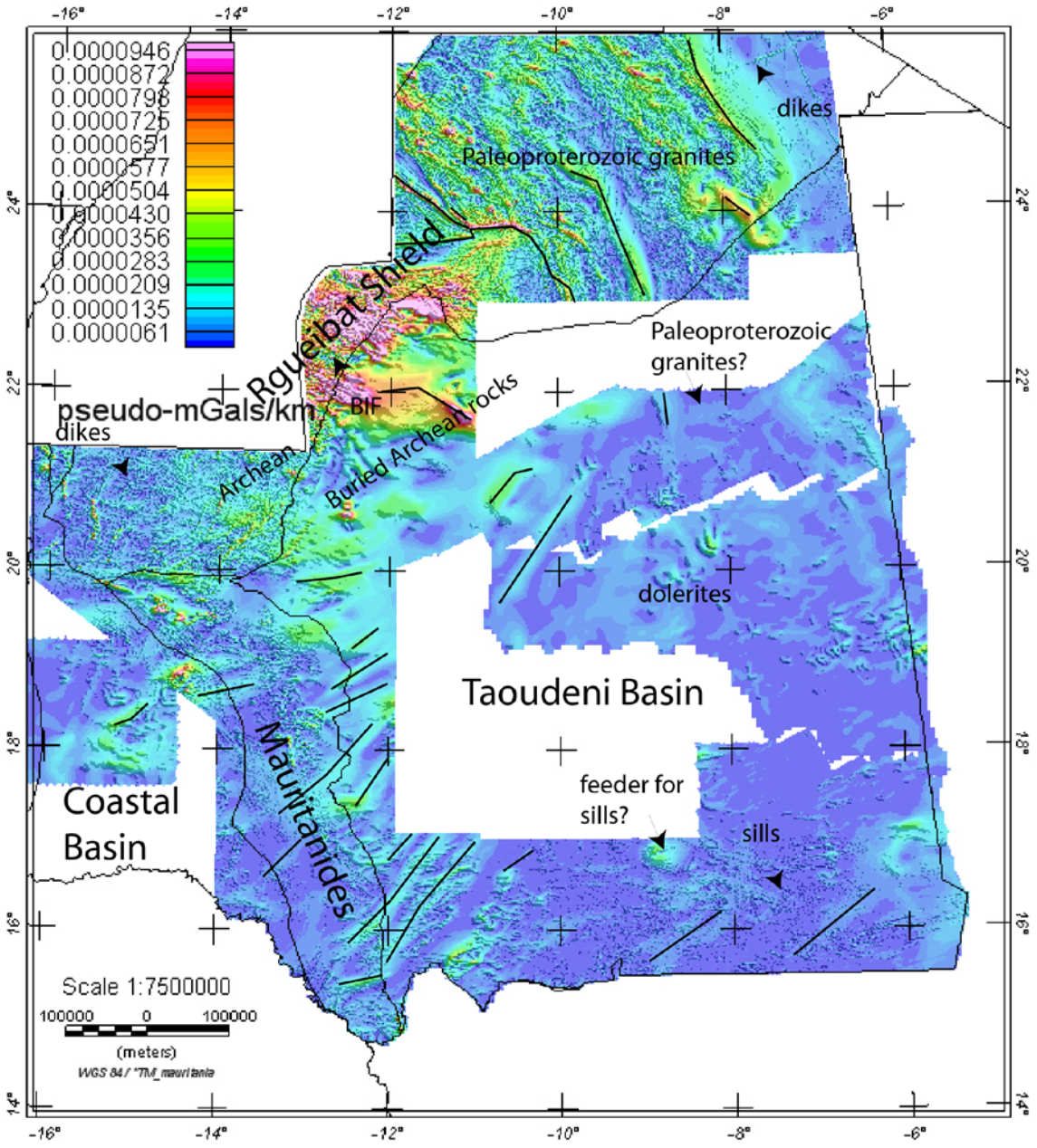

Figure 9. Color-shaded relief image of the maximum horizontal gradient of the pseudogravity data. Outlines of provinces shown. The "ridges" represent magnetic contacts such as faults, terrane boundaries or lithologic contacts. Lines on selected "ridges" indicate inferred major Precambrian boundaries.

2.2.5 Terrace Function

Terracing is a processing technique that converts smoothly varying potential field data into hard-edge domains with intra domain-variation minimized, mimicking geologic units (Cordell and McCafferty, 1989). The pseudogravity data (fig. 3) were "terraced"—the smoothly

varying potential field data were transformed into step-like functions, with the vertical segments of the steps marking the inflection points of the anomalies—that is the maximum horizontal gradient (fig. 8).

2.3 Data Interpretation

In order to determine the geologic sources of magnetic anomalies, geologic units were overlain on the RTP (figs. 1 and 2) and filtered (figs. 6–8) data in a GIS (Finn and Horton, 2015). In addition, magnetic susceptibilities were measured on representative rock types (appendix 1, Finn and Horton, 2015) and incorporated into the interpretation. Sources of narrow linear positive magnetic anomalies include dikes ranging in age from Archean-Cretaceous, Archean BIF with susceptibilities ranging from low values of 10^{-6} SI for hematite BIF to .2–.9 SI unit for magnetite BIF (appendix 1), edges of Jurassic-Triassic dolerite sills and intrusions and high frequency anomalies in the Mauritanides that may relate to serpentinized ultramafic rocks or mafic rocks trapped in mélange (figs. 1–2, 6, 8). Broader magnetic highs and lows are associated with Archean and Proterozoic granites. In general, Paleoproterozoic granites of 2,100–2,050 and 2,050–1,995 Ma (PP1 and PP3, respectively, Finn and Horton, 2015) correspond to magnetic lows. The positive anomalies seem to mostly correlate with granodiorites, but in many places, mapped granites do not have a consistent magnetic signature (some parts are highs, others lows) (PP2, 2,100–2,050 Ma, Finn and Horton, 2015). High frequency magnetic lows are associated with Archean greenstone belts and occasionally with dikes, indicating that they are reversely-magnetized. Magnetic lows are also associated with greenstone belts.

Magnetic anomalies that do not seem to have a corresponding surficial expression occur throughout the map area. Buried dikes throughout the region produce clear linear magnetic anomalies extending for hundreds of kilometers. These dikes cut across anomalies associated with the older rocks, indicating that they are most likely Jurassic in age. Many of the high frequency positive anomalies in the Mauritanides have no surficial expression, but some are associated with serpentinized peridotite. The grain of the magnetic anomalies within the Mauritanides follows the trend of the belt (fig. 2).

In the pseudogravity (fig. 3) and low frequency bandpass (fig. 7) filtered maps, the eastern part of the Rgueïbat shield is characterized by alternating 120–150 km wide, northwest trending magnetic highs (300nT, fig. 7) and lows with sources that seem to extend about 130 km under the Taoudeni Basin before disappearing. Anomalies of this trend are visible in proprietary aeromagnetic data to the north. These anomalies could represent the basement to arcs that accreted to the Archean craton in the Paleoproterozoic. Similar magnetic patterns occur over Paleozoic arcs accreted to the Precambrian continent in China and Afghanistan. Prominent high-amplitude magnetic (200–300 nT) and pseudogravity lows mark the boundary between the Archean and Paleoproterozoic granites (figs. 1–3, 7). South of the lows are very high amplitude broad east-trending magnetic (fig. 2) and pseudogravity (fig. 3) and match filtered highs (fig. 6) over Archean rocks. The source of these anomalies is not clear. Along the western and southern edge of the Taoudeni Basin are a series of northeast-trending ~50 km wide magnetic and pseudogravity (fig. 3) and filtered magnetic (fig. 7) highs and lows that are virtually uncut by the Mauritanide Belt and in some cases, extend nearly to the coast. These anomalies are not clearly visible over the Taoudeni Basin, suggesting that their source is buried too deep beneath the basin

to be observed. Positive anomalies over the Taoudeni Basin are most likely associated with Jurassic dolerite sills and feeders within the sedimentary section (figs. 2, 3 and 6). The high frequency signature (fig. 6) of this area is characteristic of volcanic rocks.

2.4 Depth to Basement Mapping

One of the most reliable methods for obtaining depths to the top of crystalline rock beneath cover is from the Extended Euler method. Employing Euler's homogeneity equation and assuming a simple magnetic source type, the lateral and vertical gradients and Hilbert transforms of the measured magnetic field can be unambiguously related to the horizontal and vertical positions of the source (Mushayandebvu and others, 2001; Nabighian and Hansen, 2001; Reid and others, 1990; Thompson, 1982). Good clustering of solutions indicates that a source location is well resolved, and poor clustering indicates solutions that should probably be ignored (Reid and others, 1990). The choice of source model, or structural index, is critical for reasonable results. The use of improper structural indices will yield solutions that are widely scattered laterally and have inaccurate depths. The structural index is directly related to the rate of the decrease of field intensity with distance from the magnetic source.

The method has been shown to be reasonably effective (as compared to other source depth estimate algorithms) at determining magnetic source depths and especially good at locating the horizontal position of sources (Reid and others, 1990). Extended Euler deconvolution represents a significant improvement over the standard method (Phillips, 2002). Within a small window size specified by the user, the number of equations is increased and computational stability is enhanced by adding the Hilbert transformations of the total-field magnetic anomalies in the horizontal directions with the horizontal and vertical magnetic gradients. Unknown constants related to regional effects are solved for and removed. This allows additional solutions to be attempted for each individual grid point, as compared to traditional Euler deconvolution. Also, a minimum depth surface (such as the surface topography) is taken into account. If a solution lies above that surface, a second inversion takes place that determines a new structural index for that solution that places it at the minimum depth surface (a higher structural index places a solution at a greater depth). In other words, spurious depth solutions are dealt with in a geophysically meaningful way and suppressed. At the end of this process, there is either (1) no solution in the window, or (2) one solution containing the average source location, the average depth error, the average structural index, and the number of components contributing to the average. Solutions produced from a large number of components are more reliable than those produced from a small number of components, as are solutions with smaller average error in depth. These two parameters can be combined in an "Euler information index." This index is high for more reliable solutions and low for less reliable solutions. Less reliable solutions should not necessarily be rejected, because many real sources are only detected in one or two of the seven components. However the index is useful for determining which solutions are the most repeatable and have the lowest error (Phillips, 2002).

Table 1. Structural indices for Euler deconvolution of magnetic anomalies (from Reid and others, 2003).

Structural Index	Geologic Model	Depth Type
0	Contact of considerable depth extent or high throw fault	Depth to top
0.5	Contact/edge/fault of intermediate relief or throw	Depth to top
1	Thin sheet edge (sill, dike, BIF, etc.) or low throw fault/contact	Depth to top
2	Line source (pipeline, narrow kimberlite pipe, etc.)	Depth to center
3	Sphere or compact body at a distance	Depth to center

Extended Euler deconvolution was applied to the raw (*not* reduced to pole) total field aeromagnetic anomalies over the Islamic Republic of Mauritania by trying each structural index listed in Table 1 and comparing the different results. Indices of 2 and 3 are not likely to represent shapes of regional sources in the magnetic data and result in unreasonably deep depths, so the likely best-fit indices are 0 and 1. A structural index of 0 is appropriate for the Taoudeni Basin (fig. 10). This index represents the minimum depth to the shallowest sources. While different indices produced better solution clustering for different source types, as should be expected, the best overall starting structural index is 1, representing the maximum depth to the shallowest sources. This index is best because most of the magnetic sources in the region are dikes, sills and banded iron formation (BIFs). Because of the large size of the dataset, it was difficult to expeditiously examine the solution clustering for many anomalies. To omit as many depth poor solutions as possible, we eliminated those whose Euler information index was below 0.4. This number was chosen based on comparing clustering and information indices for several regions. In the estimates using a structural index of 0 (fig. 10), far fewer solutions are obtained over the areas containing dikes, sills and BIFs than when using an index of 1 (fig. 6), an indication that 0 is an inappropriate index for these regions. Similarly, more solutions are found for the Taoudeni Basin using an index of 0 (fig. 10) than 1 (fig. 11; Finn and Horton, 2015). The Euler results were subtracted from the Islamic Republic of Mauritania digital elevation model to obtain depths below the surface.

In addition to the choice of structural index, several factors impact the quality of the depth estimates including the window size, accuracy of the flight elevation and topographic surfaces, and the flight line spacing. The window size must be small enough to capture features of interest but not so large as to include multiple anomalies. After many trials, the window size that gave the largest number of good solutions is 7 (3,500 m). Good solutions may be obtained but if the flight elevation and (or) topographic surfaces are poorly known, the depth estimates will be degraded. In the case of the Islamic Republic of Mauritania data, the topographic surface is poorly known in many places, and the flight elevations of the new data are probably good to within 25–50 m. For shallow sources, such as exposed rocks, depth estimates should equal zero but can deviate by as much as ~100 m, but typically less than 50 m for the Euler structural index of 0. For the structural index of 1, representing the maximum depth to the source, the depths are

generally 100–400 m too deep (fig. 11; Finn and Horton, 2015). For depth estimates exceeding ~2,000 m, the ambiguity increases and depths may only be good to about 1,000 m. Of course, for those regions with an incorrect structural index, the errors will be greater. Because we do not know the flight specifications for the U.N. data, depth estimates for regions covered by those surveys were not used for the following discussion. They will be used in the discussion of the hydrology. For the individual mineral resource assessments that use the depth estimates, we assume that regions with depths less than 1,000 m (fig. 11; Finn and Horton, 2015) might be prospective. It is likely that the magnetic sources are shallower than 1,000 m.

Another issue is whether the top of the crystalline basement coincides with magnetic basement. In the northern part of the Islamic Republic of Mauritania, the geology is largely exposed. This is reflected in the depth estimates that show the tops of most of the sources to lie within the upper 100 m of the surface for Euler structural index of 0 and 100–300 m for the structural index of 1 (fig. 11; Finn and Horton, 2015). The depths obtained are to magnetic basement, which typically, but not always corresponds to crystalline basement. In several places in the Rgueïbat shield, the magnetic data sense magnetic sources beneath non-magnetic granites at the surface, giving spurious depths to "crystalline basement." This is an unusual case where the calculated depths to magnetic sources deviate strongly from crystalline basement. In areas where the magnetic banded iron formations are altered to low magnetic susceptibility hematite (appendix 1; Finn and Horton, 2015) the depth estimates are also deep, reflecting the loss of magnetization of the surficial rocks.

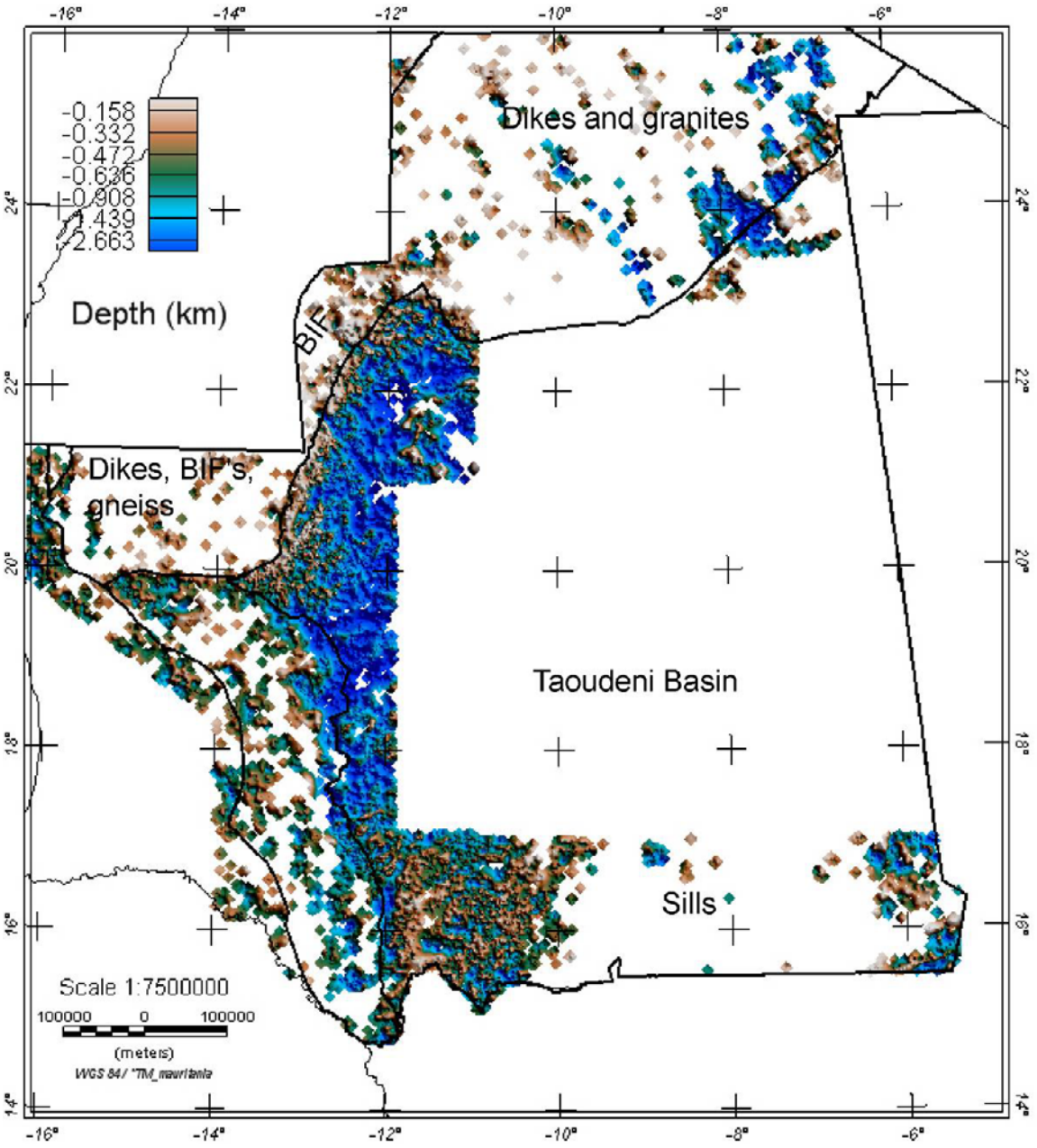

Figure 10. Color-shaded relief image of gridded estimates of the depth to magnetic sources beneath the surface using the Extended Euler method (Phillips, 2002). A structural index of 0 and a window size of 7 (3,500 m) were used.

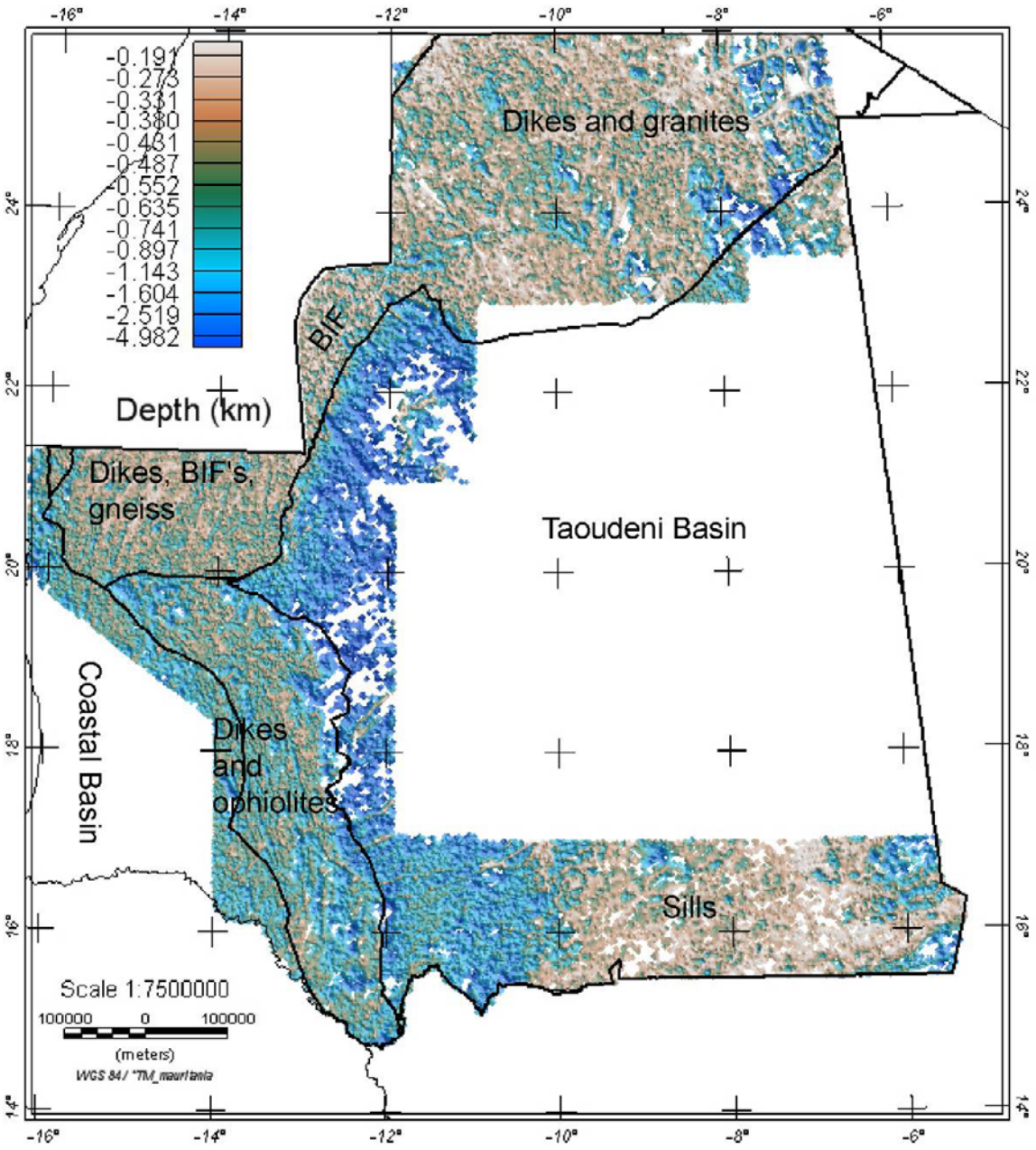

Figure 11. Color-shaded relief image of gridded estimates of the depth to magnetic sources beneath the surface using the Extended Euler method (Phillips, 2002). A structural index of 1 and a window size of 7 (3,500 m) were used.

3 Radiometric Data

While many naturally occurring elements contain radioactive isotopes, only potassium and the uranium and thorium decay series possess radioisotopes that produce gamma rays of sufficient energy and intensity to be measured by gamma ray spectrometry. This is because they

are relatively abundant in the natural environment. The actual elements measured and their units are: **K:** potassium, for example K40 (units: %), **eU:** equivalent uranium concentration by weight (the spectrometer directly measures Bi214, that is an indirect measure of uranium) (units: ppm) and **eTh**: equivalent thorium concentration by weight (the spectrometer directly measures Tl208, that is an indirect measure of thorium) (units: ppm). The depth of penetration of the radioelement data is about 30 cm, so it is most valuable as a surficial geologic mapping tool. Average crustal abundances of these elements quoted in the literature are in the range 2–2.5% K, 2–3 ppm U, and 8–12 ppm Th (Nicolet and Erdi-Krausz, 2003).

The radiometric data were collected along with the aeromagnetic data and reduced by the contractors (FUGRO and Sanders). The gridded K, Th, and U data from the 1:200,000 scale sheets were merged together (figs. 12–14) and added together to produce a ternary radioelement map (fig. 15; Finn and Horton, 2015). A ternary radioelement map is a color composite image generated by modulating the red, green, and blue phosphors of the display device or yellow, magenta and cyan dyes of a printer in proportion to the radioelement concentration values of the K, Th, and U grids. The use of red, green, and blue for K, Th and U, respectively, is standard for displaying gamma ray spectrometric data. Blue is used to display the U channel, since this is the noisiest channel and the human eye is least sensitive to variations in blue intensity. White regions contain high concentrations of all three elements, whereas blue and other dark colors indicate low concentrations of all three elements. Although radiometric data were collected with the magnetic data in the U.N. Surveys (fig. 1), they are total count and not individual element data so are not included in figs. 12–15.

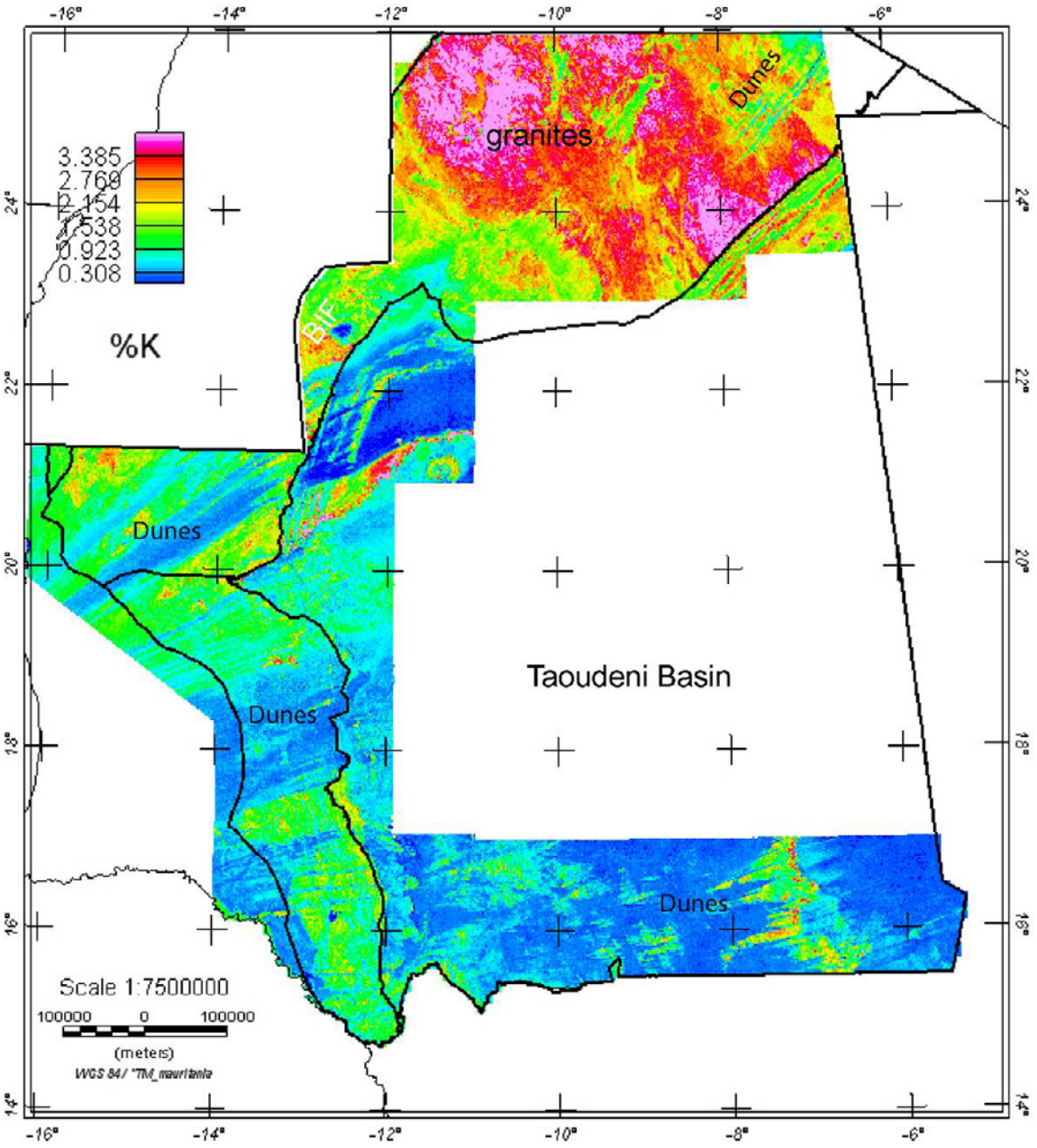

Figure 12. Color image of Potassium (%) data.

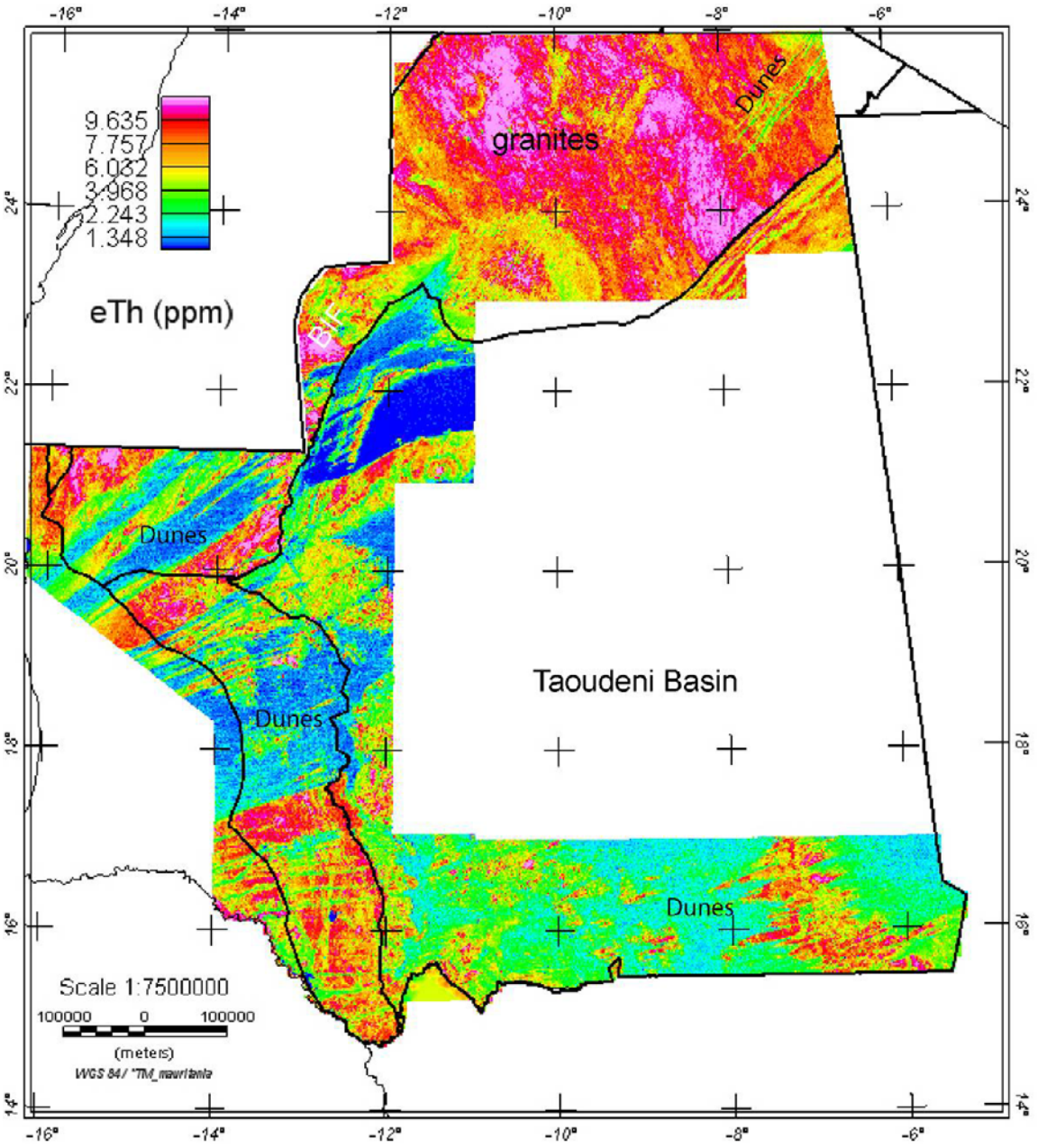

Figure 13. Color image of Thorium (ppm) data.

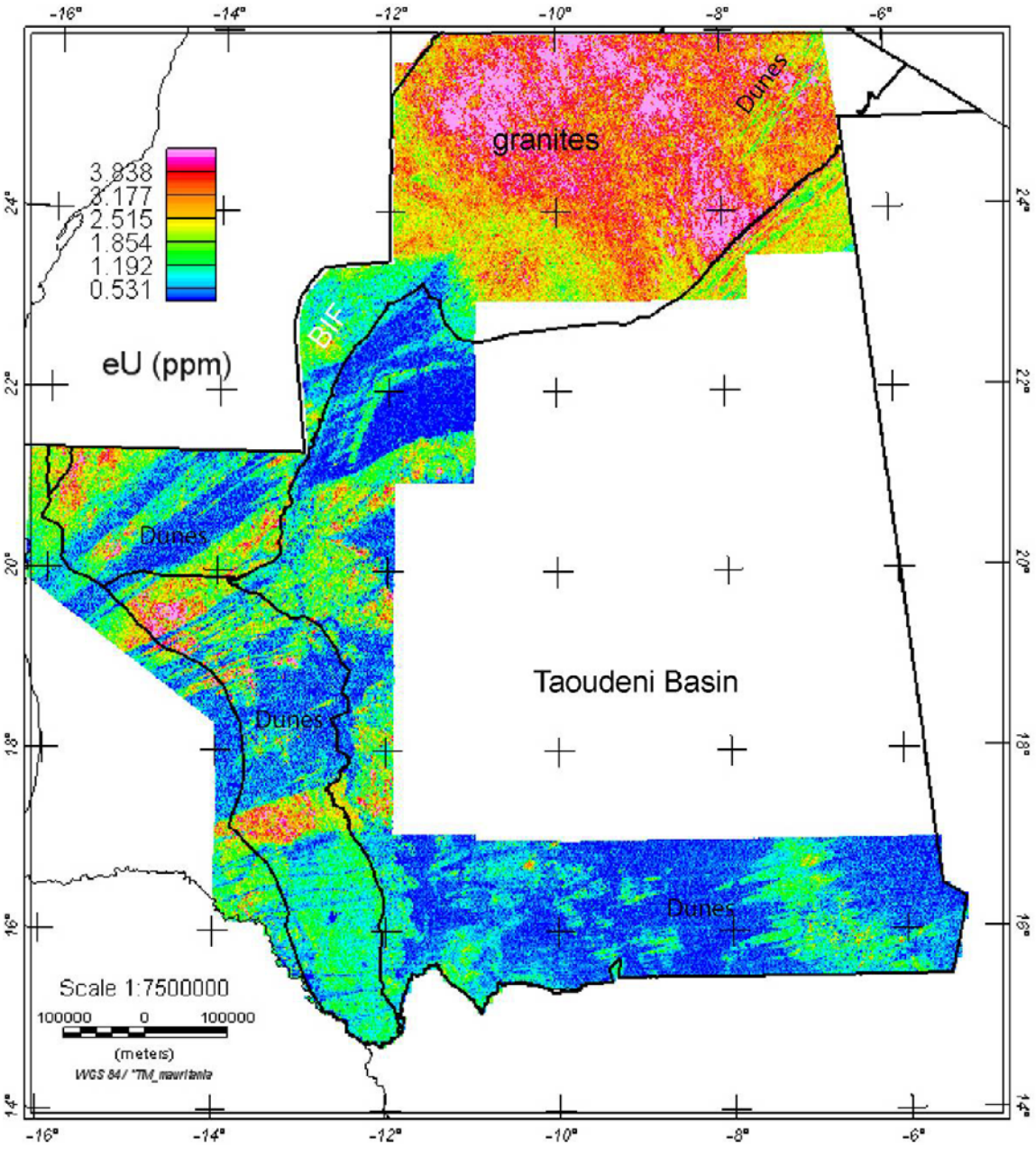

Figure 14. Color image of Uranium (ppm) data.

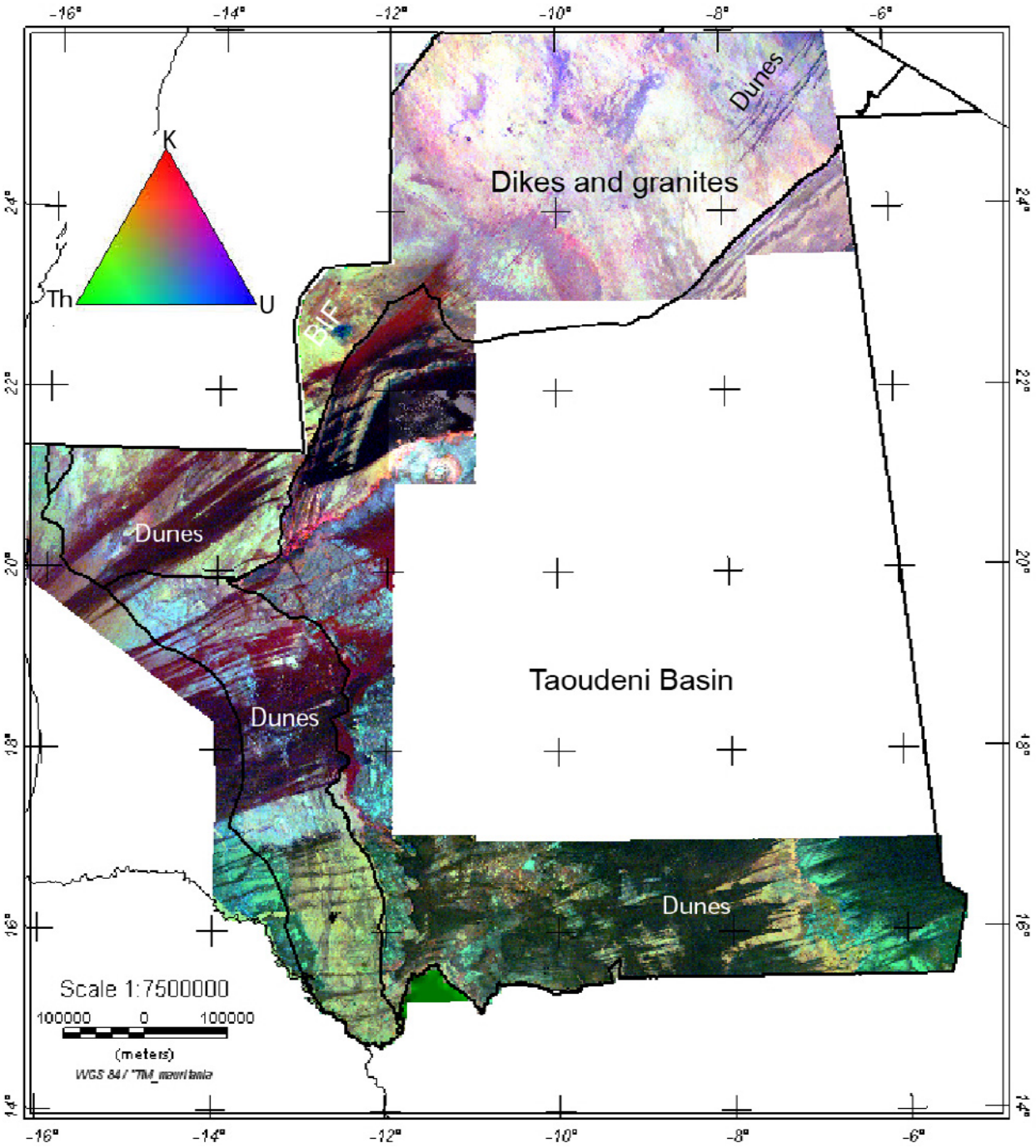

Figure 15. Color composite image red = K, green = Th, and blue = U.

All radiometric images show the highest radioelement values over the Paleoproterozoic granitic portion of the Rgueïbat Shield, which is not surprising. The sharp boundaries visible in all the radiometric data (figs. 12–15) between this province and adjacent Archean rocks corresponds to a fault, (not a survey) boundary and is not an artifact of merging the datasets. Other older basement areas are also high in radioelement concentration with the thorium

showing high values over mapped mafic rocks. The variation in radioelement concentration in the sand dunes from the north to the west to the south suggests a variable sediment source for the sands. The radioelement data are useful for mapping the surficial geology, in particular, the ternary element map (fig. 15; Finn and Horton, 2015). In this map, for example, the Ordovician sedimentary rocks on the western edge of the Taoudeni Basin produce bluish colors on the ternary map. Details about chemical variations within the sedimentary section can be obtained from this map. However, with the exception of mapping variations in the chemistry of the exposed Precambrian units, some banded iron formations and dikes in the Rgueïbat Shield variations in the radioelement data do not correspond to the magnetic data (fig. 1).

4 Geologic Basement Maps

A crystalline basement and structure maps were constructed from the geophysical data. A crystalline Precambrian-Jurassic basement map comprises the residual from the upward continuation process (fig. 8; Finn and Horton, 2015) and the bandpass filtered residual for the U.N. data (fig. 9; Finn and Horton, 2015). In addition to imaging lithologies of igneous and metamorphic units, it is also a structure map in that it is dominated by the signature of dikes, BIFs, and ophiolites in the north and west and sill boundaries in the Taoudeni basin. A structure map was constructed with the gray shade of the reduced to the pole magnetic data and mapped structures (fig. 17; Finn and Horton, 2015). The features on this map span the Archean to Jurassic, but do not contain Paleozoic features as no rocks that age are magnetic (Finn and Horton, 2015). The magnetic anomalies were used to extend the interpretation of mapped geology (Finn and Horton, 2015) and structure (Finn and Horton, 2015) under cover and is constrained by susceptibility measurements (appendix 1). The gray shade map (fig. 17) shows small scale fractures, BIFs and dikes that are a proxy for structure (Finn and Horton, 2015). Large scale new lineaments, mostly dikes, were generated from the magnetic data and added to the mapped structures (Finn and Horton, 2015).

4.1 Crystalline Basement Map

High-frequency magnetic anomalies (fig. 8; Finn and Horton, 2015) are almost a direct proxy for the crystalline geology, especially at the 1:1,000,000 scale. Therefore, we use them directly as a geologic map (fig. 16) and provide a key to interpretation of them (Finn and Horton, 2015). The upward continuation residual map (fig. 8) represents the high frequency anomalies in the new data better than the other filters (for example, figs. 6 and 9) because it retains the largest amount of high frequency information. Some noise is retained in the data but does not unduly alias the anomalies. In contrast, because of the lower resolution of the U.N. data, the upward continued residual anomaly data contains noise such that anomalies are aliased. For the basement map covered by the U.N. data, we used the bandpass filtered data (fig. 6), because the noise was filtered out. The upward continued residual data (fig. 8) and filtered U.N. data (fig. 6) were placed together in an image (not analytically merged) used for the crystalline basement map (fig. 16; Finn and Horton, 2015). The depth to the top of the interpreted crystalline basement is shown in fig. 11, and Finn and Horton, 2015. Types of anomalies visible on the map are discussed below in terms of their geologic sources determined from comparison with the geologic map and magnetic data over other Precambrian shields. As the scale of the entire map (fig. 16) is too

small to easily see small anomalies, insets (figs. 18–30) are used in the following discussion along with the 1:1M map (Finn and Horton, 2015). A more regional view follows the detailed discussion below.

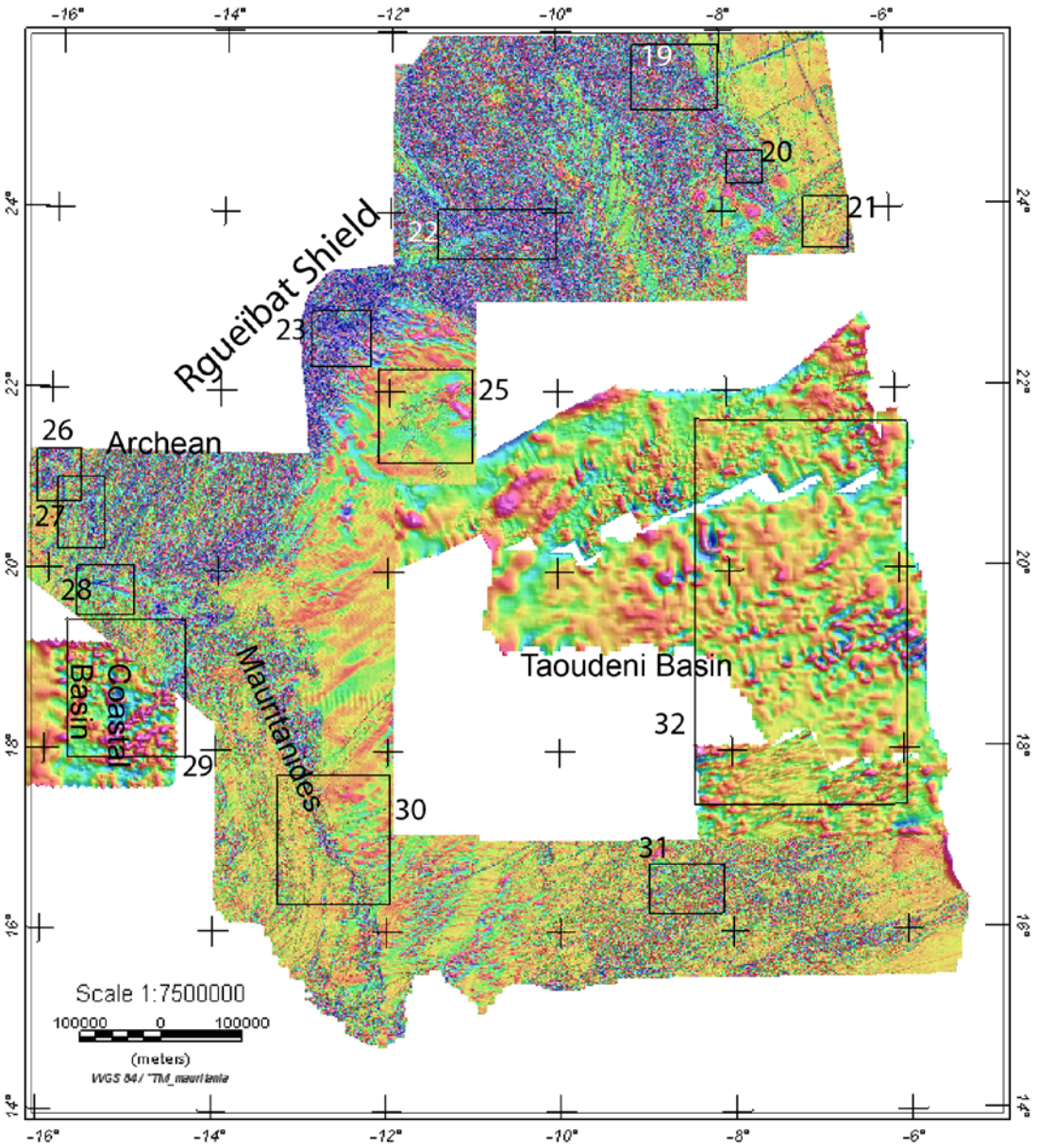

Figure 16. Crystalline basement map derived from residual map derived from subtracting the upward continued (by 100 m) reduced to pole magnetic data from the original reduced to pole (fig. 1) data (fig. 8) and bandpass filtered U.N. data (fig. 6). Numbered boxes refer to figures in the text. See Finn and Horton, 2015 for correlation of magnetic anomalies with selected geologic units and susceptibility measurements.

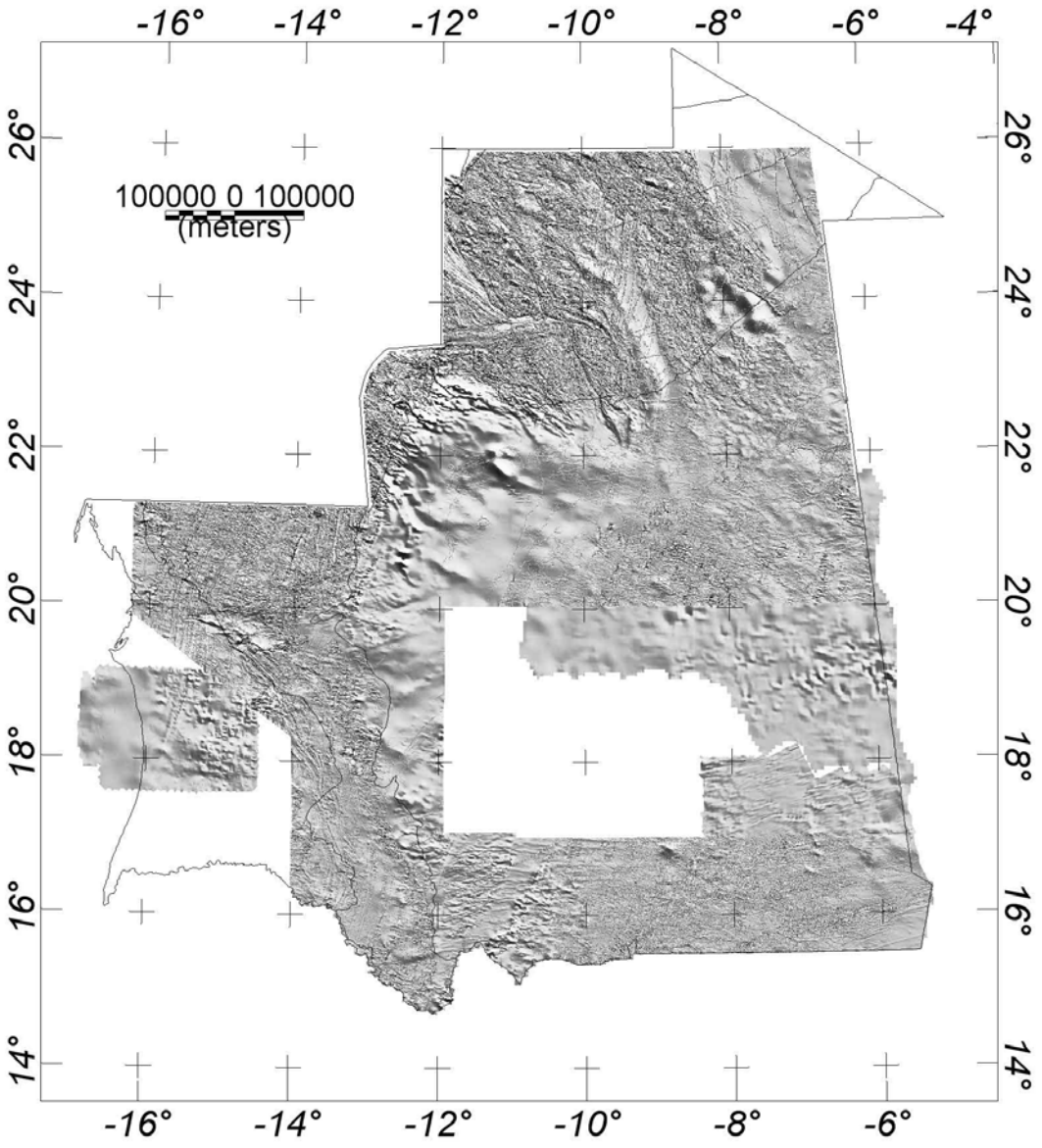

Figure 17. Gray shade reduced to the pole magnetic map of all data. Finn and Horton, 2015 shows mapped structures along with those derived from this map.

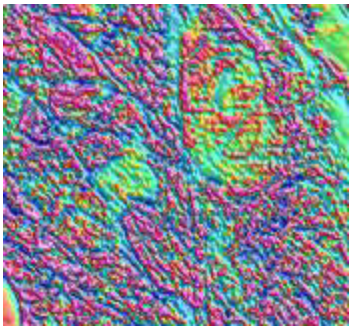

Figure 18. Close-up of crystalline basement map over fractured Paleoproterozoic granite (fig. 16; Finn and Horton, 2015).

Interpreted fractures within granites produce short (20–100 km) linear positive and negative anomalies with amplitudes ranging from ~50–300 nT (fig. 18). The circular pattern in the upper right most likely represents compositional zonation within a small pluton. A similar pattern is observed in the ternary radiometric data (fig. 15, Finn and Horton, 2015). Calculated depths to the top of magnetic basement (fig. 11; Finn and Horton, 2015) range from ~50–400 m.

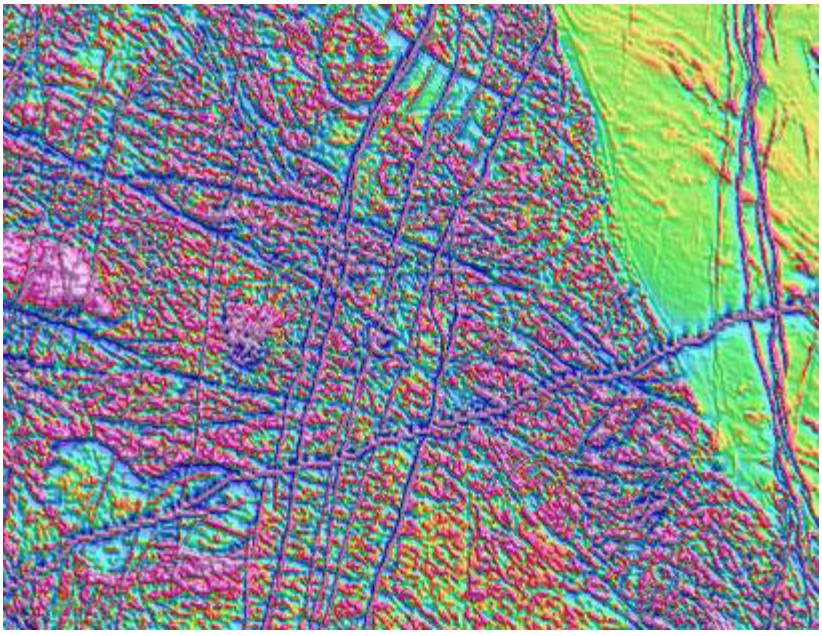

Figure 19. Close-up of crystalline basement map over dikes in the northeastern portion of the Rgueïbat Shield.

Long (hundreds of km), linear north, NE, and SW trending positive and negative anomalies characterize dikes in the Rgueïbat Shield (fig. 19). The SW trending dike anomaly crosses all other anomalies, indicating that it is younger. The shorter linear anomalies associated with fractures can clearly be differentiated from the dikes (Finn and Horton, 2015). The variation in anomaly intensity from west (high) to east (low) indicates variations in magnetite content of the mapped granites whose susceptibilities range from 0036 (magnetic quiet zone on the east) to 22 x 10^{-3} SI units in the more magnetic granites and granodiorites elsewhere (Paleoproterozoic granites, appendix 1). Calculated depths to the top of magnetic basement (fig. 11; Finn and Horton, 2015) range from ~50–500 m.

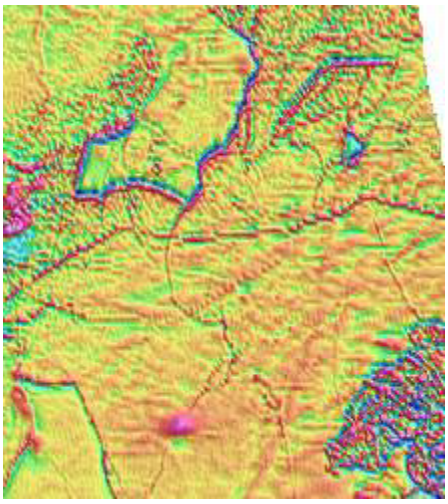

Figure 20. Close-up of crystalline basement map over Triassic-Jurassic sills and volcanic rocks at the northern border of the Taoudeni Basin (box 20, fig. 16; Finn and Horton, 2015).

Edges of Triassic-Jurassic sills within the Taoudeni Basin produce characteristic linear anomalies arranged in polygons—often as low-high pairs (fig. 20). High frequency anomalies (SE corner of map) typically characterize Triassic-Jurassic volcanic rocks whose susceptibilities range from 15–33 x 10^{-3} SI (dolerites, microgabbros, appendix 1). Calculated depths to the top of magnetic basement (fig. 11; Finn and Horton, 2015) range from ~50–1.5 km in the southwest.

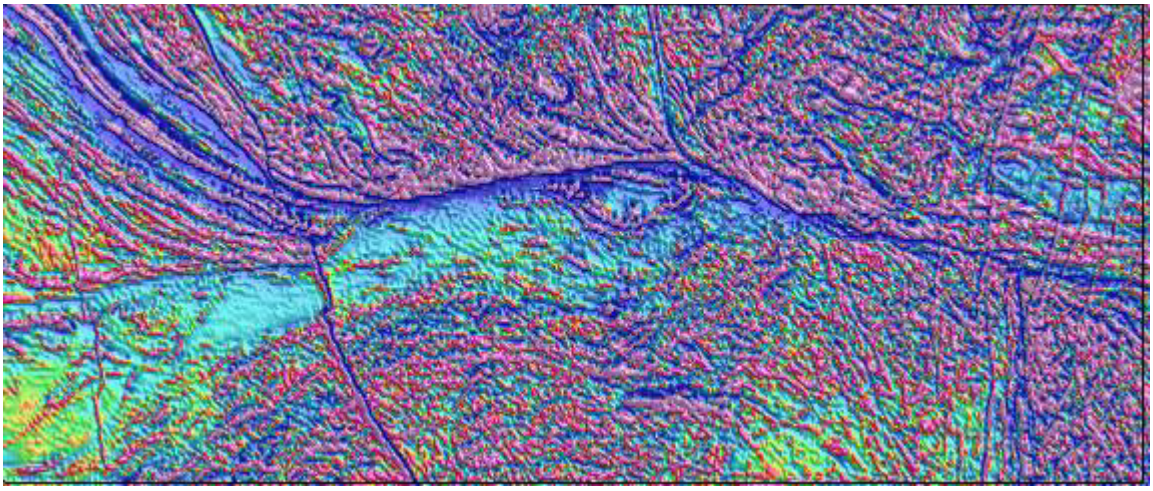

Figure 21. Close-up of crystalline basement map over the Archean (south)-Paleoproterozoic boundary (north) (box 21, fig. 16, Finn and Horton, 2015).

A linear east-trending magnetic low characterizes the Zednes fault that marks the boundary between the Archean (south) and Paleoproterozoic rocks (north) (fig. 21). Easterly anomaly trends associated with BIFs in the south are truncated by the low associated with the fault. Linear anomalies crossing this boundary indicate younger dikes. BIFs occur within the fault zone (Finn and Horton, 2015). Other faults in the region are also lows. Age relations can be determined by examination of anomaly relations. Calculated depths to the top of magnetic basement (fig. 11; Finn and Horton, 2015) range from ~60–800 m.

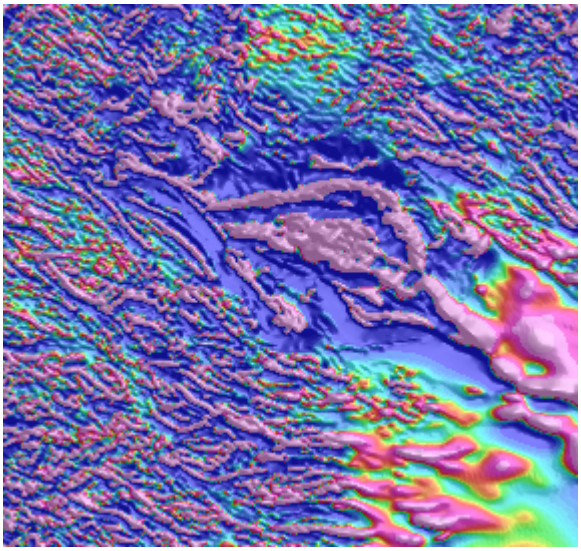

Figure 22. Close-up of crystalline basement map over BIFs in F'Derick (box 22, fig. 16; Finn and Horton, 2015).

BIFs produce short (tens of km) narrow wavy high amplitude (>500 nT–3,000 nT) positive magnetic anomalies (fig. 22). The BIFs act as structural markers within deformed non-magnetic greenstone belts. They can be differentiated from all other anomaly sources by the very high amplitudes of the anomalies that they produce. The broad, high amplitude anomalies in the center correspond to the Paleoproterozoic Kediat Ijil complex whose susceptibilities range from 0.027 x 10^{-3} SI in the hematites to 570 x 10^{-3} SI in the magnetite bearing units (Compex d'Ijil, appendix 1; O'Connor and others, 2005). In addition, the Kediat Ijil is associated with low concentrations of radioelements (figs. 12–15). The longer wavelength anomalies in the SE portion of the map correspond to BIFs beneath the Taoudeni Basin. The gneissic and granitic basement are magnetically quiet, with susceptibilities <~50 x 10^{-3} SI (appendix 1 and (O'Connor and others, 2005). Calculated maximum depths to the top of magnetic basement in this region (fig. 11, Finn and Horton, 2015) is less than ~1,000 m.

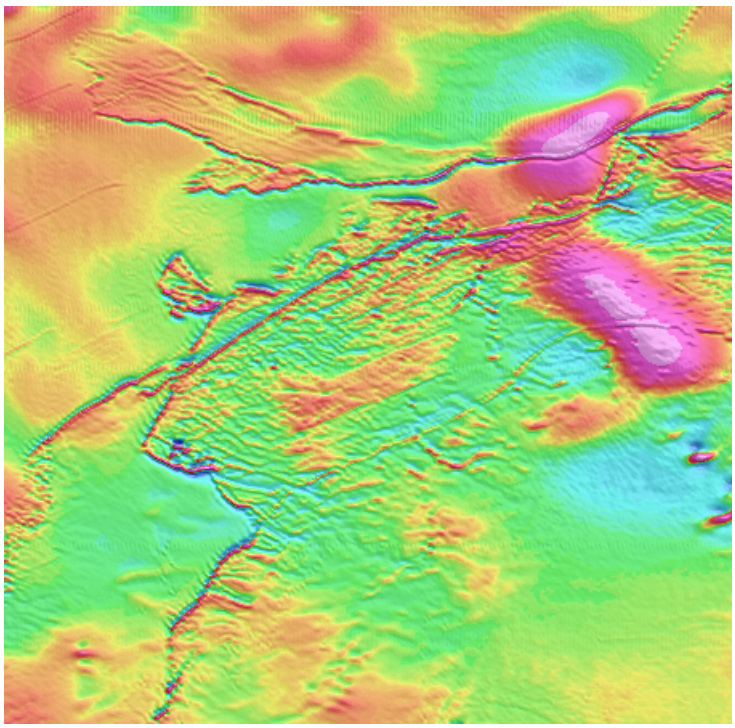

Figure 23. Close-up of crystalline basement map over Triassic-Jura ssic sills and volcanic rocks at the western border of the Taoudeni Basin (box 23, fig. 16; Finn and Horton, 2015).

Linear, undulating paired magnetic highs and lows mark the edges of Triassic-Jurassic sills at the western edge of the Taoudeni Basin whose susceptibilities range from 15–33 x 10^{-3} SI (dolerites, micrograbbros, appendix 1). These anomalies cross broad wavelength positive anomalies presumably due to deeper sources (fig. 23). Calculated depths to the top of magnetic basement (fig. 11; Finn and Horton, 2015) range from ~20–400 m for the shallow sill sources and > 5,000 m for the broad anomalies.

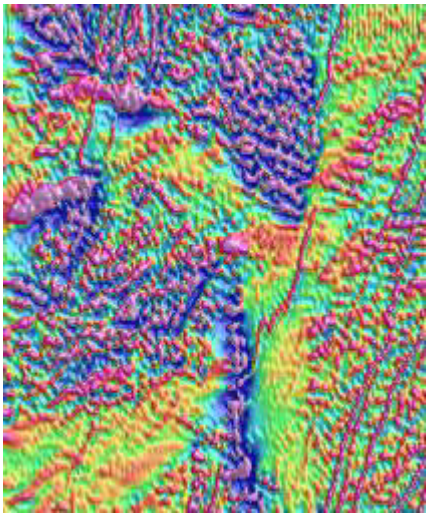

Figure 24. Close-up of crystalline basement map over the northern boundary between the Mauritanide belt (high frequency anomalies on west) and Archean BIFs and Triassic-Jurassic dikes (east) (box 24, fig. 16; Finn and Horton, 2015).

High frequency generally east-trending anomalies associated with the Mauritanide belt clearly truncate more northerly (NNW, NNE) trending anomalies of the Archean BIFs and Jurassic dikes (fig. 24). The anomalies within the Mauritanide belt most likely relate to slivers of ophiolite and (or) deformed BIF. Calculated depths to the top of magnetic basement (fig. 11; Finn and Horton, 2015) range from ~100–900 m.

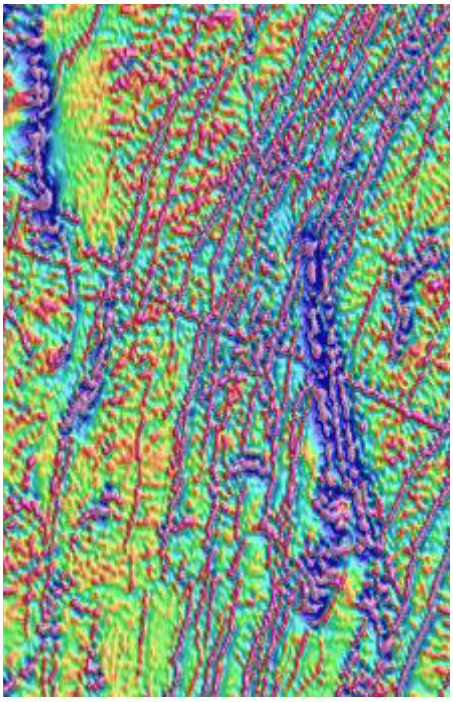

Figure 25. Close-up of crystalline basement map over Archean gneiss domes or BIF (linear and circular NNW trending highs) and greenstone belts (high amplitude lows) (box 25, fig. 16; Finn and Horton, 2015).

North-northwest trending bands of circular and linear magnetic highs embedded in high amplitude magnetic lows can be observed in the southern portion of the exposed Archean basement (fig. 25). The sources of the highs are BIFs (fig. 1). The BIFs are low in potassium (fig. 12), thorium (fig. 13) and with moderate concentrations of uranium (fig. 14) so appear blue on the ternary radiometric map (fig. 15; Finn and Horton, 2015). Linear anomalies related to younger (Cretaceous?) dikes cross these anomalies. Calculated depths to the top of magnetic basement (fig. 11; Finn and Horton, 2015) range from ~150–700 m.

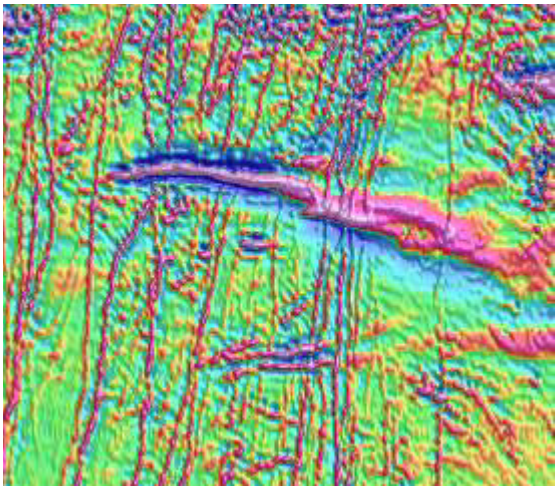

Figure 26. Close-up of crystalline basement map over north-central portion of Mauritanide belt (east-trending linear high of unknown origin) and younger dike anomalies (box 26, fig. 16; Finn and Horton, 2015**).**

A high amplitude east-trending magnetic high characterizes the northern end of the exposed Mauritanide chain (fig. 26). The source of the anomaly is buried, but other east-trending anomalies seem also to be associated with the Mauritanide deformation of Archean BIF ((Meyer and others, 2006). These anomalies are crossed by northerly trending highs associated with Jurassic dikes related to the opening of the Atlantic. Calculated depths to the top of magnetic basement (fig. 11, Finn and Horton, 2015) range from ~200–700 m for the dikes and ~1,500 m for the BIF source.

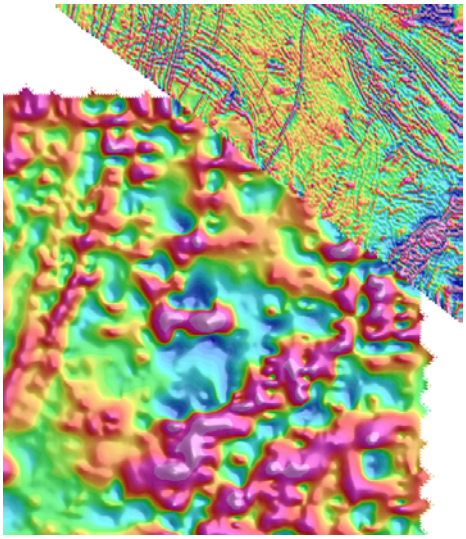

Figure 27. Close-up of crystalline basement map over the Coastal Basin (box 27, fig. 16; Finn and Horton, 2015).

The broader line spacing of the U.N. data over the sediment-covered Coastal Basin compared to the new data is apparent in the broad wavelengths of the anomalies (fig. 27). The positive anomalies most likely relate to Cretaceous dikes and perhaps unknown older basement (NE-trending high in SE portion of map). Calculated depths to the top of magnetic basement (fig. 33) are not well determined because of broad line spacing and uncertain flight height, but range from ~350 in the north east- >4,000 m at the western edge of the map.

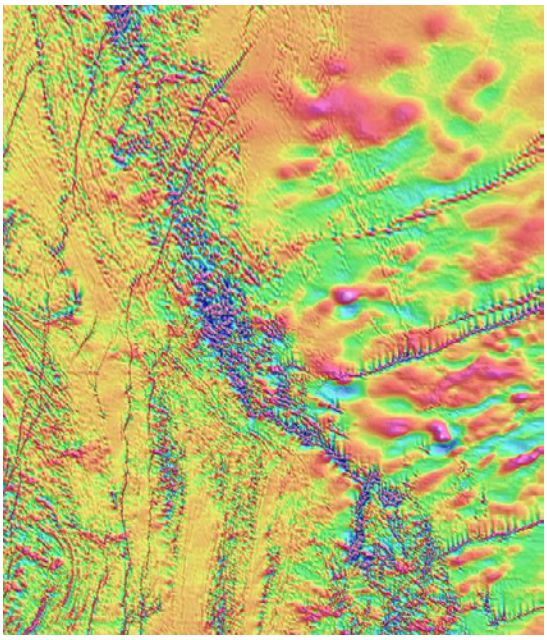

Figure 28. Close-up of crystalline basement map over the Mauritanides (box 28, fig. 16; Finn and Horton, 2015).

High-frequency east trending anomalies characterize the central portion of the Mauritanide belt (fig. 28). These small anomalies most likely relate to magnetic slivers of serpentinized ophiolite in the orogenic belt with susceptibilities as high as 141 x 10^{-3} SI (appendix 1). The linear anomalies in the western portion of the map correspond to the tectonic grain of the belt and are also reflected in the radiometric data (fig. 15; Finn and Horton, 2015). Their anomaly sources are unknown, but likely to correspond to dikes. Linear SW trending anomalies related to dikes are truncated by anomalies in the Mauritanide belt. Longer wavelength anomalies in the east most likely relate to Precambrian basement of unknown origin. Calculated depths to the top of magnetic basement (fig. 11, Finn and Horton, 2015) in the Mauritanides and west range from ~90–2,000 m. The dikes to the east are at depths of ~100–1,000 m and the deeper basement is at depths exceeding 3 km.

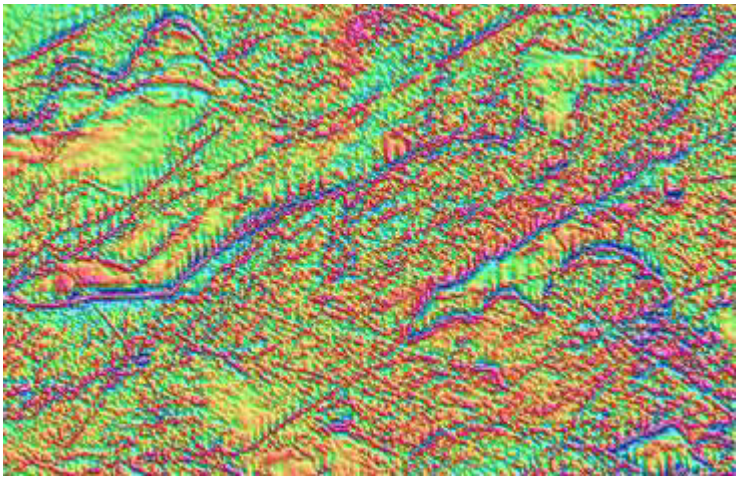

Figure 29. Close-up of crystalline basement map over Triassic-Jurassic sills and volcanic rocks at the southern border of the Taoudeni Basin (box 29, fig. 16; Finn and Horton, 2015).

An example of a dense network of Triassic-Jurassic sills at the southern edge of the Taoudeni Basin (fig. 29). Some of the straight NE-trending anomalies may relate to dikes. Calculated depths to the top of magnetic basement (fig. 11; Finn and Horton, 2015) range from ~100–500 m.

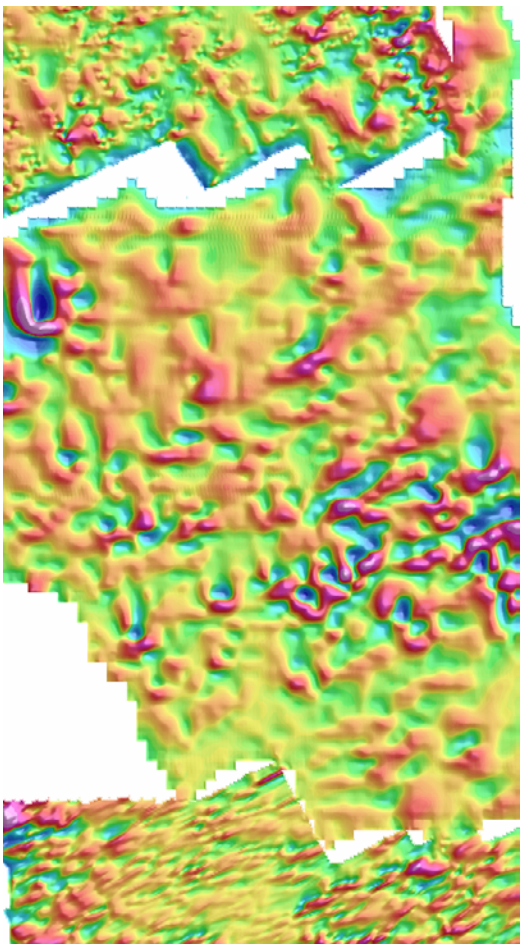

Figure 30. Close-up of crystalline basement map over Triassic-Jurassic sills and volcanic rocks in the Taoudeni Basin (box 30, fig. 16; Finn and Horton, 2015).

Various resolutions of filtered U.N. data (fig. 6) over the Taoudeni Basin contain mostly positive anomalies related to Triassic-Jurassic dolerites within the upper part of the basin that is completely covered by sand (fig. 30). The varying resolution is reflected by the varying wavelength of anomalies that are most likely at similar depths with similar sized sources. This demonstrates the aliasing of varying line-spaced data. Calculated depths to the top of magnetic basement (fig. 33) are not well determined because of broad line spacing and uncertain flight height, but range from ~350– >5,000 m.

4.2 Precambrian Basement/Tectonic Map

The detailed descriptions of significant magnetic units and correlation with surface geology and radiometric data (Finn and Horton, 2015) allow interpretation of regional geologic units (fig. 2; Finn and Horton, 2015), structures (Finn and Horton, 2015), their extensions

beneath cover up to ~5 km depth (Finn and Horton, 2015). Various low pass filters (for example, figs. 3 and 7) highlight broad sources at the expense of shallow and narrow sources like BIFs, dikes and sills. These allow interpretation of broad scale tectonic features. The latest magnetic anomaly map (Finn and Horton, 2015), along with the information in the crystalline basement map (Finn and Horton, 2015), geologic map (Bradley, Motts, and others, 2015), tectonic elements (O'Connor and others, 2005; Schofield and others, 2012), and comparisons with adjacent regional magnetic surveys (Maus and others, 2007) were used to generate a Precambrian basement map for the Islamic Republic of Mauritania (fig. 31).

Archean Terranes

The oldest rocks in the Archean terrane are 3.51 Ga orthogneisses (Potrel and others, 1996) in the Amsaga Complex, which is composed of quartzo-feldspathic migmatitic tonalitic, trondhjemitic and granodioritic gneisses as well as charnockitic gneisses with minor units of garnet–cordierite–sillimanite gneiss and basic-ultrabasic rocks (Schofield and Gillespie, 2007). An intrusion in the suture zone between the Amsaga Complex and Tasiast-Tiirit Terrane is dated at 2954±11 Ma. Magnetic highs in the Amsaga Complex are associated with magnetic pyroxenites (96 x 10^{-3} SI), some granites/granodiorites (3.75–10.235 x 10^{-3} SI) and BIFs (35 x 10^{-3} SI, appendix 1), particularly in the suture zone (fig. 2; Finn and Horton, 2015). The Amsaga Complex continues below the sedimentary cover of the Taoudeni Basin (fig. 2; Finn and Horton, 2015) and can be extended east based on similar magnetic anomalies (fig. 31 to depths of ~3 km (fig. 11, Finn and Horton, 2015) but this continuation is not well defined (fig. 2, Finn and Horton, 2015). The Tasiast-Tijirit Terrane is composed of ~2.97 Ga tonalitic and granitic gneisses interleaved with amphibolitic units interpreted as remnants of ~3.05–3.60 Ga greenstone belts (Schofield and others, 2012). The only notable magnetic units are the banded iron formations (fig. 2; Finn and Horton, 2015).

The Inchiri Complex, located on a bend in the northern part of the Mauritanides, is composed of a pile of allochthonous terranes that were thrust towards the east onto the West African Craton (Villeneuve, 2005). They are in thrust contact with the Amsaga Complex to the northeast. Basal metabasalts overlain by BIF and metasedimentary schists are separated by an unconformity from volcano-sedimentary successions that also contain BIF (Meyer and others, 2006). Recent dating suggests that these are Archean and underwent deformation at 2,492 Ma (Meyer and others, 2006). Final emplacement at the current position occurred at ~300 Ma. Broad, high amplitude magnetic anomalies associated with exposed and inferred BIFs in a magnetic quiet zone characterize the region. The width of the northern magnetic high (fig. 26) suggests BIFs that have been thrust together in a thick sequence. The buried southern and eastern extent of the province (fig. 31) is poorly defined by the magnetic data (fig. 2).

The northeastern part of the Archean terrane is underlain by the Tiris Complex, a Neoarchaean granite migmatite assemblage containing numerous units of highly magnetic (F'derick, appendix 1) ferruginous quartzite and paragneiss, metamorphosed under granulite facies conditions (Schofield and Gillespie, 2007; O'Connor and others, 2005). The ternary plot of the radiometric data indicates that the Archean rocks in the region are uniformly relatively high in radioelements and does not indicate a change in chemistry at the surface (fig. 15) within the varying magnetic signatures of the same units. Prominent linear, high amplitude magnetic

anomalies associated with BIF are associated with most of the region (fig. 22). The source of a regional magnetic high over part of the Tiris Complex (fig. 2) is not clear as the basement is generally not particularly magnetic (appendix 1; O'Connor and others, 2005). The high amplitude of the anomaly allows extrapolation of the Tiris complex beneath the Taoudeni Basin (fig. 31) to depths at least 5 km (Finn and Horton, 2015). Paleoproterozoic rocks in the Kediat Ijil and El Mahaoudat Range, a klippe of metasediments including ferruginous quartzite, capped by a distinctive conglomerate unit (Schofield and Gillespie, 2007), produce very prominent, broad, high amplitude anomalies (fig. 2, Finn and Horton, 2015) that can be extended at least 150 km beneath the Taoudeni Basin to depths >2,000 m (Finn and Horton, 2015; fig. 31).

The Zednes Suite is composed of tonalitic plutons and gneiss dated at around 3,044±5 Ma and by 2,915±18 and 2,832±4 Ma granite-granodiorites (Lahondère and Le Métour, 2003; Schofield and others, 2012) and are structurally contiguous with granitic gneisses and magnetic ferruginous quartzites of the Tiris Complex (Schofield and others, 2012). Moderate to low amplitude anomalies transected by linear lows and highs related to dikes and fractures characterize the Zednes Suite (Finn and Horton, 2015). The magnetic signatures allow extension of the unit beneath the Taoudeni Basin (fig. 31). The Temmimichate-Tsabaya Complex, the boundary between Archean and Proterozoic terranes, is composed of granulite facies, basic to ultrabasic, meta-igneous rocks and low potassium (fig. 12) and thorium values (fig. 13) mark the Temmimichate-Tsabaya Complex. The east-trending component of the Temmimichate-Tsabaya Complex is a magnetic quiet zone with high amplitude positive anomalies associated with BIF (fig. 21; Finn and Horton, 2015). The southeast trending portion of the complex is marked by a linear magnetic low and sinuous magnetic highs (Finn and Horton, 2015) that can be extended under the Taoudeni Basin to depths <1,000 m (Finn and Anderson, 2015; Taylor and others, 2015) (fig. 31).

In the northeast portion of the map where sources are exposed, the alternating magnetic highs and lows (fig. 2; Finn and Horton, 2015) relate to the granitic batholiths with varying magnetic properties and ages (Finn and Horton, 2015). Magnetic granitoids (Proterozoic granite, appendix 1) generally fall into the 2,100–2,050 Ma age range (PP2, Finn and Horton, 2015; fig. 31). Magnetite-poor granites (Paleoproterozoic granite, granodiorite, appendix 1) with 2,050–2,000 and 2,050–1,995 Ma ranges and are mixed with magnetite poor greenstones, especially in the east (PP1 and PP3, respectively, Finn and Horton, 2015, outlines; fig. 31). White to pale regions in the radiometric data (Finn and Horton, 2015) indicate the granites whereas bluer colors are associated with the greenstones. A prominent, linear magnetic low (between PP1 and PP2, Finn and Horton, 2015) extends 175 km over the Taoudeni Basin. Magnetic highs (eastern PP3, fig. 31; Finn and Horton, 2015) extend over the Taoudeni basin and link to prominent highs over Mali (Maus and others, 2007). These anomalies could relate to a ~300 km extension of the Proterozoic granites beneath ~4 km (Finn and Horton, 2015) of cover (fig. 31). Alternatively some of the highs over the Taoudeni Basin could relate to dolerite intrusions within the sedimentary sequence.

The completely buried sources that cause the observed ~50 km wide northeast-trending alternating highs and lows (figs. 2, 3, and 7) that characterize the west side of the Taoudeni Basin and central Mauritanides are unknown Precambrian basement (fig. 31). Depth estimates obtained from Euler analysis of the low-pass match filtered data (fig. 6) yielded generally poor solutions. However, a few good solutions on the anomalies suggest that they are buried 3 to less than or

equal to 4 km deep. An Archean age found in the central Mauritanides (~17^{o}45'N), suggests that the sources of the anomalies could be Archean in age. However, the amplitude, wavelength and trend of the alternating highs and lows are completely different from those associated with exposed Archean craton to the north. They are associated with corresponding gravity highs and lows (fig. 35) that have been associated with the West African Craton (Roussel and Lesquer, 1991). Major buried magnetic contacts were delineated from the maximum horizontal gradient map (lines, fig. 8). The NW trend is parallel to those trends observed in gravity (fig. 35) data as well in the magnetic data to the east in Mali (Maus and others, 2007) and south in Liberia (Behrendt and Wotorson, 1974). Given the Archean age found in the central Mauritanides and the Archean age assigned to sources in Liberia (Behrendt and Wotorson, 1974), Sierra Leone and the western Ivory coast (Strangway and Vogt, 1970) for similar magnetic and gravity anomalies, the sources could be Archean, but this is not certain. The alternating low-high character of the belt suggests granite-greenstone belts or shear zones (lows) in magnetic rocks if the rocks are Archean. There is a suggestion that similar linear highs (figs. 3 and 7) with a slightly shallower ENE trend (fig. 8) are present over the southeast portion of the Islamic Republic of Mauritania as well (fig. 6). These anomalies are largely obscured by those related to the extensive near surface sills and are lumped with the basement (fig. 31). A problem with correlating Archean aged rocks in the Mauritanides with those under the Taoudeni Basin is that the rocks in the Mauritanides are allochthonous and the linear anomalies clearly relate to in situ basement. In addition, the Archean rocks are associated with gravity highs (fig. 35), instead of alternately highs and lows as over exposed Paleoproterozoic rocks and unknown basement. Therefore, the linear magnetic anomalies could relate to Paleoproterozoic batholiths as exposed in the Kédougou-Kénieba and Keyes Inliers directly to the south in Senegal and Mali, respectively (Rocci and others, 1991). If so, Paleoproterozoic granitoid belts wrap around at least two sides of the Archean core of the Rgueïbat shield.

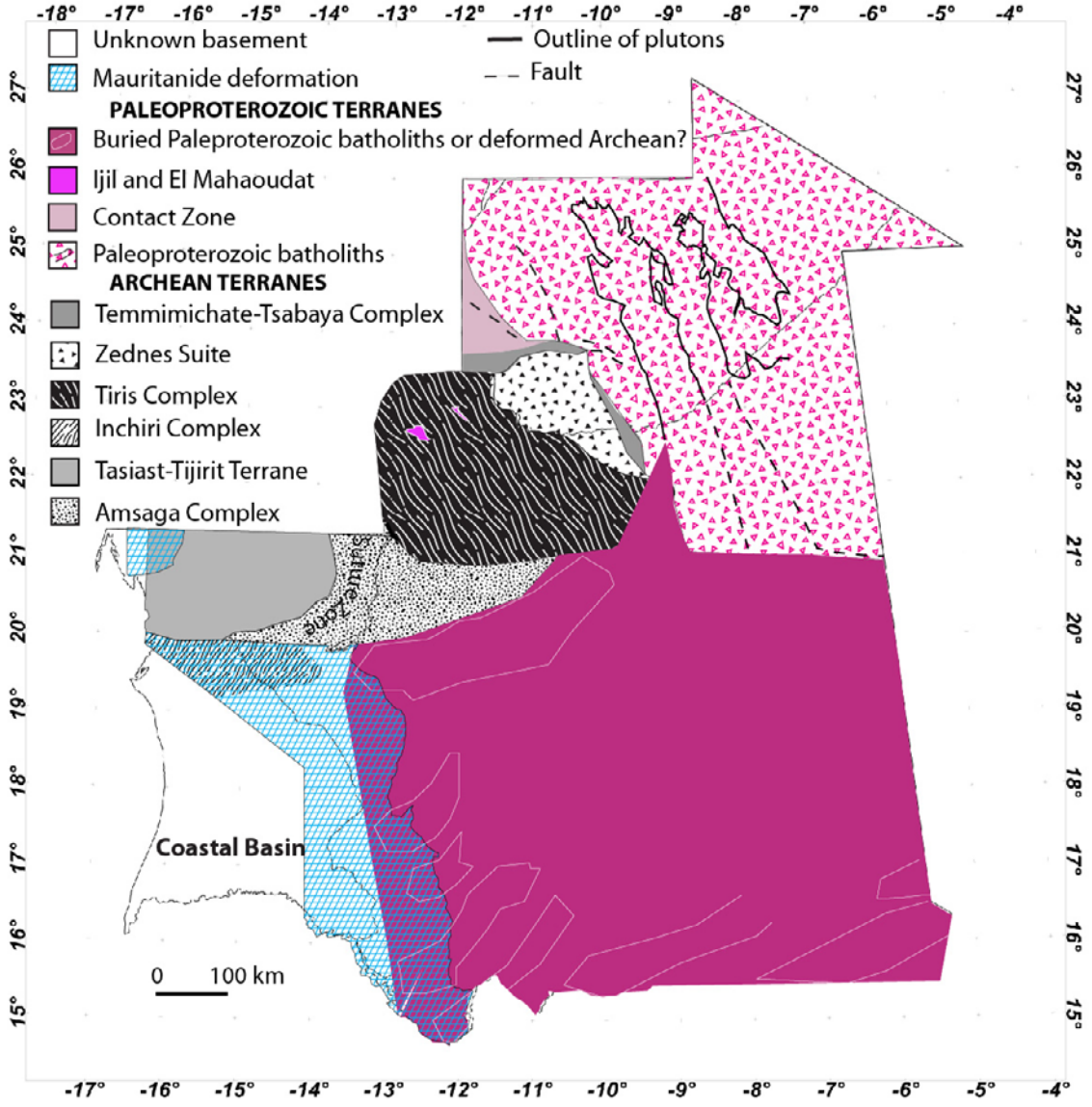

Figure 31. Precambrian basement interpreted from magnetic (Finn and Horton, 2012a), low-pass filtered magnetic (fig. 8) data and geologic mapping (for example, O'Connor and others, 2005; Schofield and Gillespie, 2007).

5 Aeromagnetic and Gravity Data for Evaluating Hydrologic Resources

A more detailed discussion of the relation of geophysical data to hydrology is in a hydrology report (Friedel and others, 2015). Radiometric data (fig. 15; Finn and Horton, 2015) reflect the distribution of dune ridges and valleys. The valleys are occasionally prospective for groundwater. Basins with sufficient depth are necessary to host aquifers. The primary basins in the Islamic Republic of Mauritania are the Taoudeni and Coastal Basins with small parts of the Tindouf Basin in the north (fig. 32). Depth estimates from the merged new and U.N. data over

the Coastal and Taoudeni Basins calculated using a structural index of 0 and a window of 7 produce depth estimates that must be treated with care (fig. 33). Depth estimates from the more widely spaced U.N. data seem to be ~1 km deeper than those from the newer data. The magnetic depth estimates indicate that Taoudeni Basin depth increases rapidly from ~500–1 km at the edge to greater than 2 km within 25 km of the edge. The greatest depths are >6 km in the areas not covered by dolerite sills. The minimum depth to the Precambrian basement in the center of the basin is ~2,900 m as determined by the Abolag-1 well (fig. 34). Depths to the Jurassic sills are ~0.5– 1.5 km, in reasonable agreement with the seismically determined thickness of the Devonian section over which the sills lie (fig. 34). The southern region covered by the magnetic data is covered by sand and sills underlain by sedimentary rocks that could source aquifers. Maximum depth estimates (Euler structural index of 1) from the southeastern portion of the basin demonstrate a pattern of shallow estimates over dolerites and deeper over basins (fig. 35). The boundary between regions of shallow and deeper estimates corresponds to a boundary between dry and aquifer areas delineated by nuclear magnetic resonance and DC electrical resistivity data (Bernard and others, 2004). The magnetic sources lie much deeper (>2,000 m, fig. 35) than the magnetite-poor clay base of the aquifer sandstones (at ~300 m depth, Bernard and others, 2004), the pattern of depth estimates may indicate regions where thick sandstones have aquifer potential (fig. 35) and can be used to target future hydrogeophysical studies.

Another possible target for groundwater is the Coastal Basin. Magnetic data cover only part of the region, with the largest part of the Coastal Basin covered by U.N. data. The depth estimates over the coastal basin from the magnetic data suggest depths of 2–3 km in the center deepening to 3–4 km along the coast in the south and north (fig. 33).

Proprietary gravity data (M. Albouy, written comm., 2007) help identify basins (fig. 36). Several ~40 km wide, linear 20–35 mGal gravity lows over the Coastal Basin indicate the location of the deepest portions of the basin. Gravity lows over the Rgueïbat shield indicate density variations within the Precambrian terrane and not basins. Several linear northeast trending gravity lows over the southwestern edge of the Taoudeni Basin are oriented in the same direction as magnetic lows (fig. 1) and have been interpreted to relate to Precambrian basement (Roussel and Lesquer, 1991) and not separate basins.

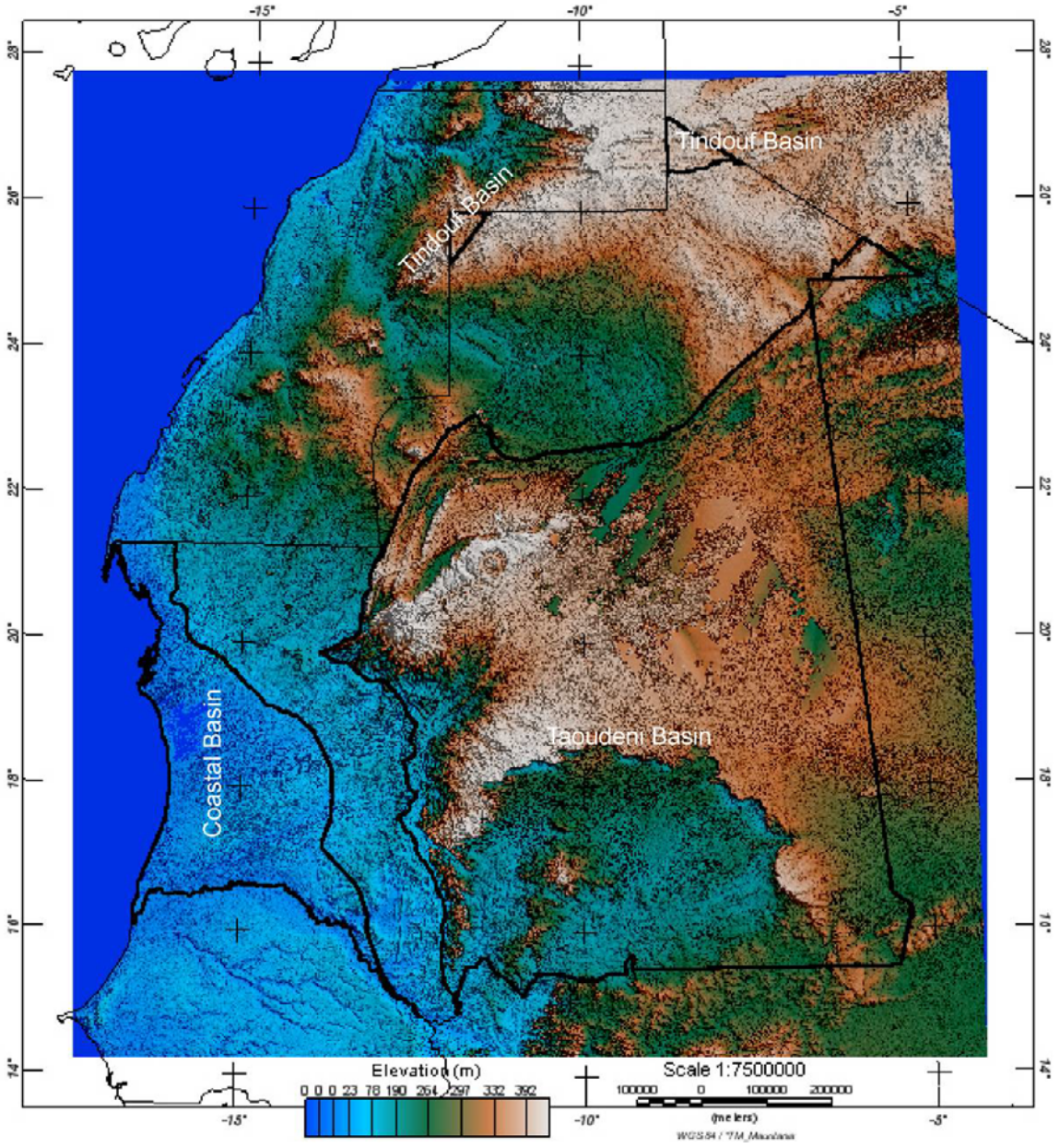

Figure 32. Color-shaded relief image of topography from SRTM and GTOPO data.

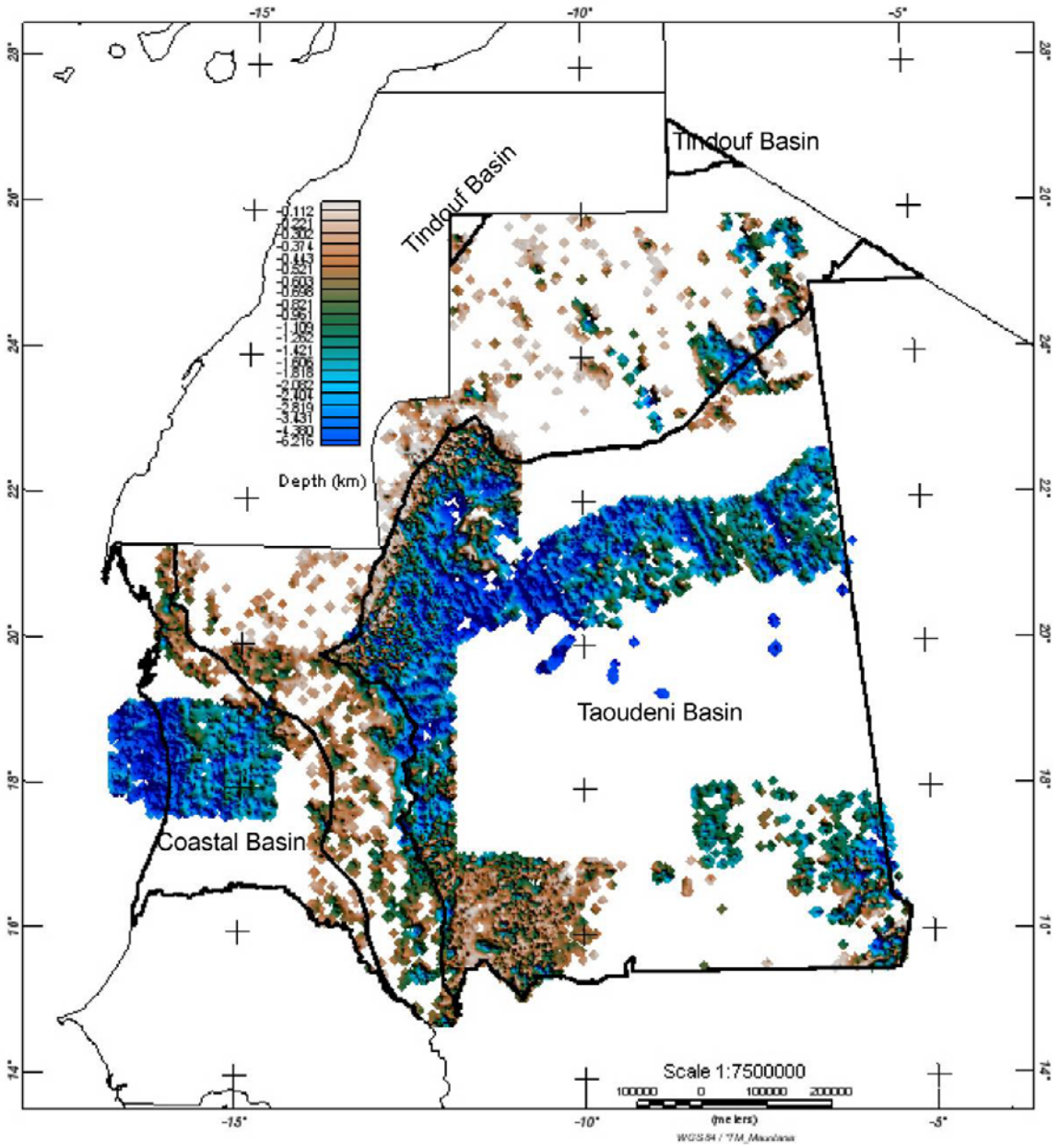

Figure 33. Color-shaded relief image of gridded estimates of depths below the surface from the merged new and U.N. data using the Extended Euler method (Phillips, 2002). A structural index of 0 and a window size of 7 (3,500 m) were used.

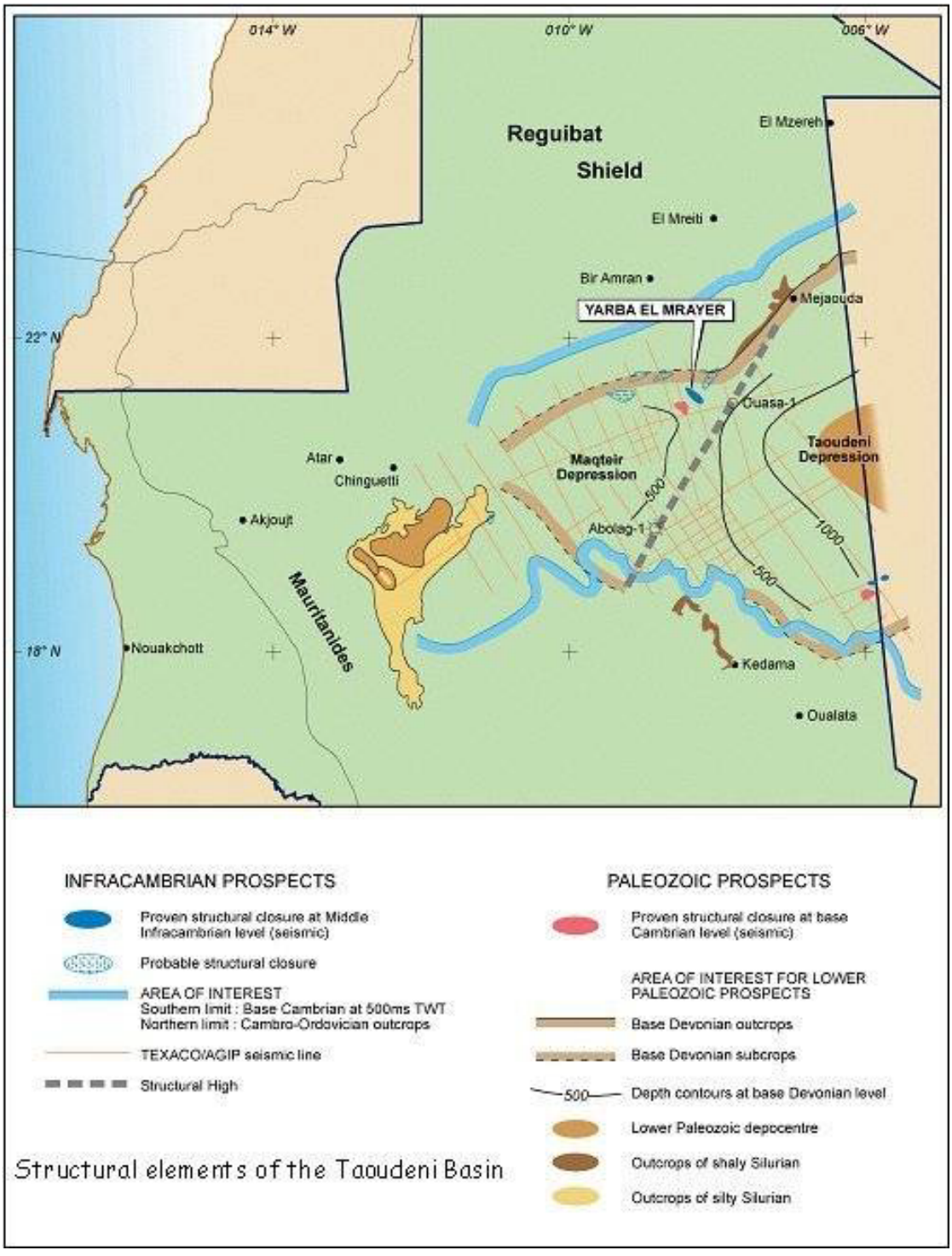

Figure 34. Map of the structural elements of the Taoudeni Basin (courtesy of the République Islamique de Mauritanie Ministère des Mines et de l'Industrie, http://www.mmi.mr/english/hydrocarbons/taoudeni.html).

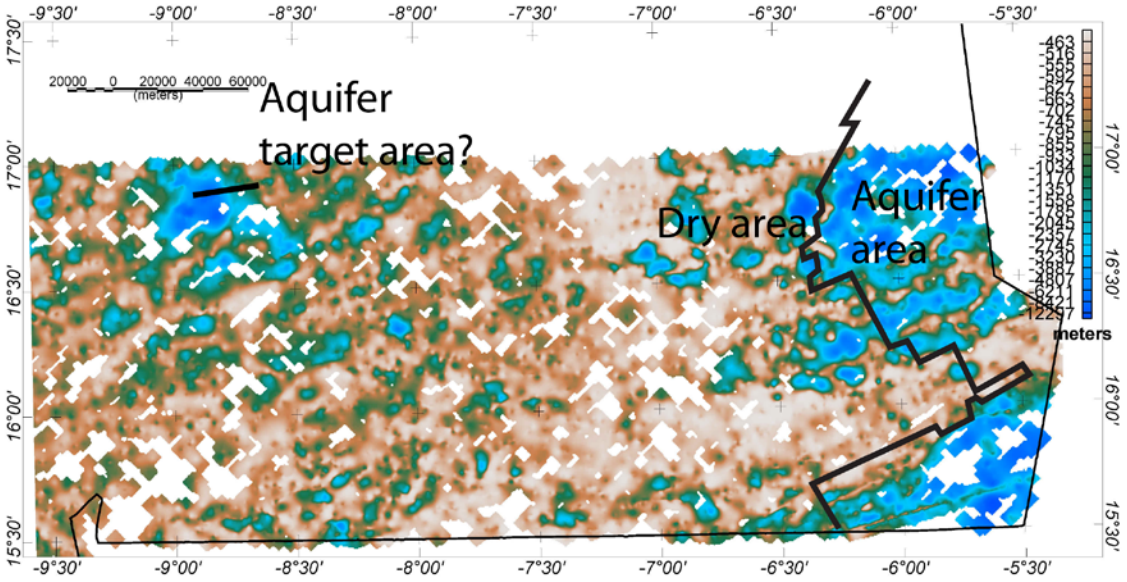

Figure 35. Color-shaded relief image of gridded estimates of the depth below the surface from the merged new and U.N. data in southeast Islamic Republic of Mauritania using the Extended Euler method (Phillips, 2002). A structural index of 1 and a window size of 7 (3,500 m) were used. The line separates dry from aquifer areas based on nuclear magnetic resonance and resistivity data (Bernard and others, 2004).

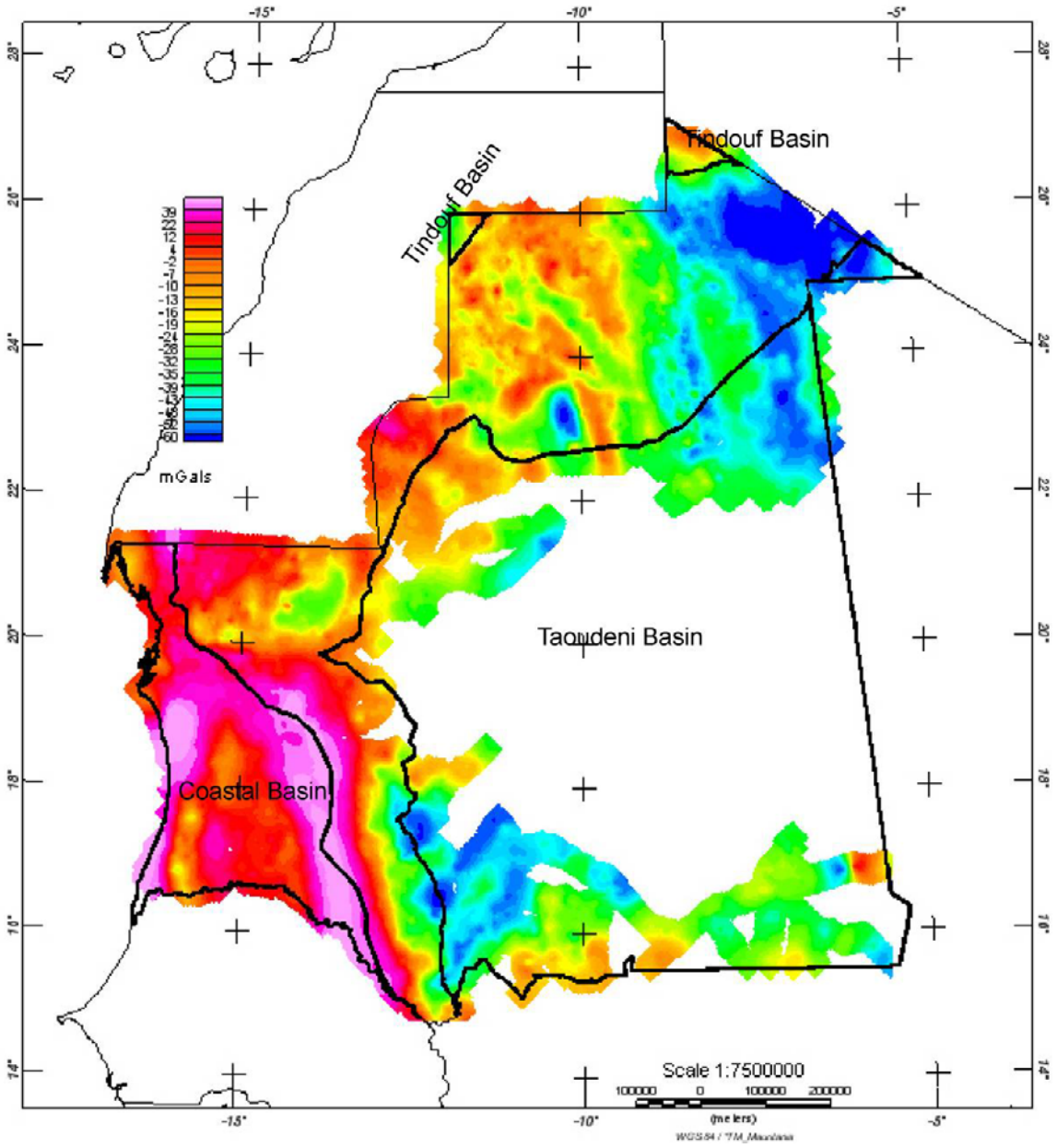

Figure 36. Simple Bouguer gravity map of the Islamic Republic of Mauritania, reduced using a density of 2.67 g/cm^3. Data courtesy of M. Albouy.

7 References

Baranov,Vladmir, and Naudy, H., 1964, Numerical calculation of the formula of reduction to the magnetic pole: Society of Exploration Geophysicists, v. 29, p. 67–79.

Bath, G.D., 1968, Aeromagnetic anomalies related to remanent magnetism in volcanic rock, Nevada Test Site: Memoir, Geological Society of America, p. 135–146.

Behrendt, J.C., and Wotorson, C.S., 1974, Geophysical surveys of Liberia with tectonic and geologic interpretations: U.S. Geological Survey Professional Paper 810, 33 p.

Bernard, J., Lemine, M., Phy, B.D., and Ricolvi, M., 2004, Combination of electrical resistivity and magnetic resonance sounding data for mapping an aquifer layer in Mauritania, Society of Exploration Geophysicists Annual Meeting, Denver, October 10–15, 2004: Society of Exploration Geophysicists, p. 6.

Blakely, R.J., 1995, Potential Theory in Gravity and Magnetic Applications: Cambridge University Press, 464 p.

Blakely, R.J., and Simpson, R.W., 1986, Short Note—Approximating edges of source bodies from magnetic or gravity anomalies: Geophysics, v. 51, no. 7, p. 1494–1498.

Bradley, D.C., Motts, H.A., Horton, J.D., Giles, Stuart, and Taylor, C.D., 2015, Geologic map of Mauritania (phase V, deliverables 51a, 51b, and 51c), chap. A1 *of* Taylor, C.D., ed., Second projet de renforcement institutionnel du secteur minier de la République Islamique de Mauritanie (PRISM-II): U.S. Geological Survey Open-File Report 2013–1280-A1, 3 pl., scale 1:1,000,000, http://dx.doi.org/10.3133/ofr20131280/. [In English and French.]

Cordell, L., and Grauch, V.J.S., 1985, Mapping basement magnetization zones from aeromagnetic data in the San Juan basin, New Mexico, *in* Hinze, W.J., ed., The utility of regional gravity and magnetic anomaly maps: Society of Exploration Geophysicists, p. 181–197.

Cordell, L., and McCafferty, A.E., 1989, A terracing operator for physical property mapping with potential field data: Geophysics, v. 54, p. 621–634.

Finn, C.A., and Horton, J.D., 2015, Crystalline basement map of Mauritania derived from filtered aeromagnetic data (phase V, deliverable 54_1), Aeromagnetic and geological structure map of Mauritania (phase V, deliverable 54_2), Maximum depth to basement map of Mauritania derived from Euler analysis of Aeromagnetic data (phase V, deliverable 54_3), and color composite image of radioelement data (added value), chap. B1 *of* Taylor, C.D., ed., Second projet de renforcement institutionnel du secteur minier de la République Islamique de Mauritanie (PRISM-II): U.S. Geological Survey Open-File Report 2013–1280-B1, 4 pl., scale 1:1,000,000, http://dx.doi.org/10.3133/ofr20131280/. [In English and French.]

Friedel, M.J., Finn, C.A., and Horton, J.D., 2015, Hydrogeologic map of the Islamic Republic of Mauritania (phase V, deliverable 56), Synthesis of hydrologic data (phase V, deliverable 57), and chemical hydrologic map of the Islamic Republic of Mauritania (added value), chap. C *of* Taylor, C.D., ed., Second projet de renforcement institutionnel du secteur minier de la République Islamique de Mauritanie (PRISM-II): U.S. Geological Survey Open-File Report 2013–1280-C, 23 p., 2 pl.,scale 1:1,000,000, http://dx.doi.org/10.3133/ofr20131280/. [In English and French.]

Grauch, V.J.S., and Cordell, L., 1987, Short Note—Limitations of determining density or magnetic boundaries from the horizontal gradient of gravity or pseudogravity data: Geophysics, v. 52, no. 1, p. 118–121.
Hansen, R.O., and Pawlowski, R.S., 1989, Reduction to the pole at low latitudes by Weiner filtering: Geophysics, v. 54, p. 1607–1613.
Lahondère, D., Thiéblemont, D., Goujou, J.-C., Roger, J., Moussine-Pouchkine, A., Le Métour, J., Cocherie, A., and Guerrot, C., 2003, Notice explicative des cartes géologiques et gîtologiques à 1/200 000 et 1/500 000 du Nord de la Mauritanie.
Maus, S., Sazonova, T., Hemant , K., Fairhead, J.D., and Ravat, D., 2007, National Geophysical Data Center candidate for the world digital magnetic anomaly map: Geochemistry, Geophysics, Geosystems, v. 8, no. 6.
Meyer, F.M., Kolb, J., Sakellaris, G.A., and Gerdes, A., 2006, New ages from the Mauritanides Belt—Recognition of Archean IOCG mineralization at Guelb Moghrein, Mauritania: Terra Nova, v. 18, p. 345–352.
Mushayandebvu, M.F., van Driel, P., Reid, A.B., and Fairhead, J.D., 2001, Magnetic source parameters of two-dimensional structures using extended Euler deconvolution: Geophysics, v. 66, p. 814–823.
Nabighian, M.N., and Hansen, R.O., 2001, Unification of Euler and Werner deconvolution in three dimensions via the generalized Hilbert transform: Geophysics, v. 66, p. 1805–1810.
Nicolet, J.-P., and Erdi-Krausz, G., 2003, Guidelines for radioelement mapping using gamma ray spectrometry data: International Atomic Energy Agency, v. IAEA-TECDOC-1363, p. 173.
O'Connor, E.A., Pitfield, P.E.J., Schofield, D.I., Coats, S., Waters, C., Powell, J., Ford, J., Clarke, S., and Gillespie, M., 2005, Notice explicative des cartes géologiques et gîtologiques à 1/200 000 et 1/500 000 du Nord-Ouest de la Mauritanie.
Phillips, J.D, 1997, Potential-field geophysical software for the PC, version 2.2: U.S. Geological Survey Open-File Report 97–725.
Phillips, J.D., 2001, Designing matched bandpass and azimuthal filters for the separation of potential-field anomalies by source region and source type: Australian Society of Exploration Geophysicists, 15th Geophysical Conference and Exhibition, expanded abstracts, CD-ROM, p. 4.
Phillips, J.D., 2002, Two-step processing for 3D magnetic source locations and structural indices using extended Euler or analytic signal methods: Society of Exploration Geophysicists, 2002 Technical Program Expanded Abstracts, v. 21, p. 727–730.
Potrel, Alain, Peucat, J.J., Fanning, C.M., Auvrey, B.M., Burg, J.P., Caruba, Christiane, 1996, 3.5 Ga old terranes in the West African Craton, Mauritania: Journal of the Geological Society London, v. 153, p. 507–510.
Reid, A.B., Allsop, J.M., Granser, H., Millett, A.J., and Somerton, I.W., 1990, Magnetic interpretation in three dimensions using Euler deconvolution: Geophysics, v. 55, p. 80–91.
Reid, A.B., 2003, Short note—Euler magnetic structural index of a thin bed fault: Geophysics, v. 68, issue 4, http://library.seg.org/doi/abs/10.1190/1.1598117.
Rocci, G., Bronner, G., Deschamps, M., 1991, Crystalline Basement of the West African Craton, *in* Dallmeyer, R. D., Lécorché, J.P., eds., The West African orogens and circum-Atlantic correlatives: Berlin, Springer Verlag, p. 31–61.

Roussel, J., and Lesquer, A., 1991, Geophysics and the crustal structure of West Africa, *in* Dallmeyer R.D., and Lecorché, J.-P., eds., The West African orogens and circum-Atlantic correlatives: Berlin, Springer Verlag, p. 9–28.

Schofield, D.I., and Gillespie, M.R., 2007, A tectonic interpretation of "Eburnean terrane" outliers in the Regüibat Shield, Mauritania: Journal of African Earth Sciences, v. 49, p. 179-186.

Schofield, D.I., Horstwood, M.S.A., Pitfield, P.E.J., Gillespie, M., Darbyshire, F., O'Connor, E.A., and Abdouloye, T.B., 2012, U-Pb dating and Sm-Nd isotopic analysis of granitic rocks from the Tiris Complex—New constraints on key events in the evolution of the Regüibat Shield, Mauritania: Precambrian Research, v. 204–205, p. 1–11.

Strangway, D.W., and Vogt, P.R., 1970, Aeromagnetic tests for continental drift in Africa and South America: Earth and Planetary Science Letters, v. 7, p. 429–435.

Taylor, C.D., Finn, C.A., Anderson, E.D., Joud, M.Y., Taleb, M. A., and Horton, J.D., 2015, Algoma-, Superior-, and oolitic-type iron deposits of the Islamic Republic of Mauritania (phase V, deliverable 83), chap. O *of* Taylor, C.D., ed., Second projet de renforcement institutionnel du secteur minier de la République Islamique de Mauritanie (PRISM-II): U.S. Geological Survey Open-File Report 2013–1280-O, 94 p., http://dx.doi.org/10.3133/ofr20131280/. [In English and French.]

Thompson, D.T., 1982, EULDPH—A new technique for making computer-assisted depth estimates from magnetic data: Geophysics, v. 47, p. 31–37.

Villeneuve, Michel, 2005, Paleozoic basins in West Africa and the Mauritanide thrust belt: Journal of African Earth Sciences, v. 43, p. 166–195.

Appendix 1

Table 2. Magnetic susceptibility measurements from the Islamic Republic of Mauritania.

Sample No.	200K Sheet	Latitude	Longitude	Altitude (m)	Lithology	Unit name	Susceptibility $X10^{-3}$ SI
EA07RIM20	FDERIK	22.88471	-12.32354	241.1		Complexe de Tiris	891
EA07RIM19	FDERIK	22.9578	-12.055	346		Complexe d'Ijil	570
CT07RIM30-1	FDERIK	22.88464	-12.32358	211.2	magnetite IF	Tiris complex-Mirikli Fm	551
EA07RIM21	FDERIK	22.8827	-12.32243	372.7		Complexe de Tiris	550
CT07RIM33-4	FDERIK	22.67806	-12.45953	487	hematite IF	Ijil Complex-Tazadit Fm	205
EA07RIM09	FDERIK	22.67439	-12.45913	386.7		Complexe d'Ijil	180
CT07RIM31-1	FDERIK	22.88272	-12.32242	349.9	magnetite IF	Tiris complex-Mirikli Fm	177
EA07RIM41	MOUDJERIA	17.4921	-12.91589	89.7		Groupe de Gadel	141
CT07RIM33-1	FDERIK	22.67858	-12.45877	483.1	hematite IF	Ijil Complex-Tazadit Fm	103
CT07RIM21_3	ATAR	21.08333	-13.16667	204	banded norite-pyroxenite	Amsaga Complex-AMIg	96.2
CT07RIM33-5	FDERIK	22.67766	-12.4597	489.4	hematite IF	Ijil Complex-Tazadit Fm	92.6
CT07RIM21_2	ATAR	21.08333	-13.16667	204	banded chromitite-norite	Amsaga Complex-AMIg	71.5
EA07RIM53	MBOUT	16.99103	-12.76522	98.8		Groupe de Gadel	65
DB07RIM47a	FDERIK	22.7055	-12.51691	0	tuff		63
CT07RIM32-2	FDERIK	22.63929	-12.43961	442.6	hematite-quartzite BIF	Ijil Complex-Tazadit Fm	61.1
EA07RIM50	MBOUT	16.99041	-12.62539	97.3		Groupe de Gueneiba	57
CT07RIM34-2	FDERIK	22.69385	-12.4786	667.3	hematite IF	Ijil Complex-Tazadit Fm	56.3
CT07RIM29-1	FDERIK	22.94087	-12.0396	315.2	magnetite IF	Ijil Complex-Mhouidat Unit	55.8
EA07RIM56	MBOUT	16.7175	-12.4848	81.5		Groupe de Gadel	40
CT07RIM20_1	ATAR	20.57438	-13.47667		chromite-bearing ultramafic	Amsaga Complex-AMIg	38.7
DB07RIM33a	FDERIK	22.67159	-12.46702	0	magnetite IF		36.2
EA07RIM25	FDERIK	22.67865	-12.45891	462.1		Complexe d'Ijil	35.5
CT07RIM01_01	AKJOUJT	19.79111	-14.38969	147.1	banded iron formation	Atomai Fm	35

Table 2. Magnetic susceptibility measurements from the Islamic Republic of Mauritania.—Continued

Sample No.	200K Sheet	Latitude	Longitude	Altitude (m)	Lithology	Unit name	Susceptibility $X10^{-3}$ SI
CT07RIM21_1	ATAR	21.08333	-13.16667	204	semi-massive chromitite in pyroxenite	Amsaga Complex-AMIg	34.3
CT07RIM32-6	FDERIK	22.6399	-12.43944	431.7	hematite-quartzite BIF	Ijil Complex-Tazadit Fm	33.1
EA07RIM34	EL_MREITI	23.2597	-7.43193	290		Groupe de l'Azlaf	31.5
EA07RIM64	SELIBABI	15.07202	-12.06609	107.6		Cortäge de MbÇdia Achar	30
CT07RIM32-5	FDERIK	22.6399	-12.43944	431.7	hematite-quartzite BIF	Ijil Complex-Tazadit Fm	29.9
EA07RIM49	MBOUT	16.99228	-12.69497	96.4		Groupe de Gadel	27.9
CT07RIM03_01	AKJOUJT	19.85233	-14.45901	117	banded iron formation	Eizzene Fm	25.7
DB07RIM50a	GLEIBAT_TENEBDAR	24.82926	-10.5547	0	granite	Leglaya Gp-Gtog	24.7
CT07RIM05_01	AKJOUJT	19.70952	-14.35029	134.4	massive magnetite-goethite-malachite		23.5
EA07RIM29	BEL_GUERDAN	25.1483	-10.1302	287.9		Complexe de Tsalabia el Khadra	22.1
CT07RIM32-1	FDERIK	22.63862	-12.43968	451.1	hematite-quartzite BIF	Ijil Complex-Tazadit Fm	20.2
EA07RIM54	MBOUT	16.88543	-12.71646	108.2		Groupe de Gadel	20
CT07RIM32-3	FDERIK	22.63953	-12.43956	434.4	hematite-quartzite BIF	Ijil Complex-Tazadit Fm	17.3
DB07RIM36a	FDERIK	22.68599	-12.54027	0	conglomeratic HIF	Ijil Complex-Seyala Fm	15.7
EA07RIM08	ATAR	21.27012	-13.15618	230.7		Complexe díAmsaga	15.7
CT07RIM38-1	EL_MREITI	23.26009	-7.43173	287.3	microgabbro	Md	15.5
EA07RIM22	FDERIK	22.64525	-12.44578	532.9		Complexe d'Ijil	15.1
CT07RIM24_1	ATAR	21.26979	-13.15568	255.7	anorthosite	Amsaga Complex-Amch	14.7
DB07RIM40a		0	0	0	quartzite		14.6
CT07RIM42-1	GUELB_ER_RICHAT	21.06853	-11.45719	383.3	gabbro		14.4
CT07RIM36-6	FDERIK	22.69007	-12.47592	455.7	hematite-quartzite IF	Ijil Complex-Tazadit Fm	14.1

Table 2. Magnetic susceptibility measurements from the Islamic Republic of Mauritania.—Continued

Sample No.	200K Sheet	Latitude	Longitude	Altitude (m)	Lithology	Unit name	Susceptibility $X10^{-3}$ SI
EA07RIM47	MBOUT	16.88771	-12.66831	88.8		Groupe de Gadel	14
CT07RIM32-4	FDERIK	22.63985	-12.43949	430.8	hematite-quartzite BIF	Ijil Complex-Tazadit Fm	13.7
EA07RIM61	MBOUT	16.16753	-12.25421	47.7		Groupe de Gueneiba	12
EA07RIM23	FDERIK	22.6407	-12.43977	432.9		Complexe d'Ijil	10.8
CT07RIM18_1	ATAR	20.42381	-13.52062	175.1	granodiorite	Amsaga Complex	10.2
DB07RIM69a	MBOUT	16.98177	-12.63972	0	quartzite/dolomite	Gueneiba Gp	9.89
CT07RIM25_1	ATAR	21.25933	-13.15357	261.7	anorthosite	Amsaga Complex-Amlb	9.86
DB07RIM32_1a	ATAR	21.08348	-13.16768	0	anorthosite		9.54
EA07RIM27	FDERIK	22.6939	-12.47839	671.2		Complexe d'Ijil	9.25
EA07RIM65	SELIBABI	15.07181	-12.0659	111.9		Cortäge de MbÇdia Achar	9
CT07RIM36-2	FDERIK	22.69007	-12.47592	455.7	hematite IF	Ijil Complex-Tazadit Fm	7.89
EA07RIM17	FDERIK	22.92157	-12.01116	329.8		Complexe d'Ijil	7.74
CT07RIM36-1	FDERIK	22.69007	-12.47592	455.7	hematite IF	Ijil Complex-Tazadit Fm	7.05
CT07RIM36-3	FDERIK	22.69007	-12.47592	455.7	hematite IF	Ijil Complex-Tazadit Fm	6.02
CT07RIM36-4	FDERIK	22.69007	-12.47592	455.7	hematite IF	Ijil Complex-Tazadit Fm	5.32
EA07RIM33	BLEKHZAYMAT	24.49623	-7.41052	376		Groupe de Blekhzaymat	5.25
DB07RIM21b	ATAR	20.004038	-13.903794	0	granite	Amsaga Complex	5.21
CT07RIM35-2	FDERIK	22.6894	-12.52959	732	high grade HIF	Ijil Complex-Seyala Fm	3.78
DB07RIM09a	AKJOUJT	19.97572	-14.37881	0	granite	Amsaga Complex-AMGn2	3.75
CT07RIM28_5	FDERIK	22.95836	-12.05477	306.3	hematite-quartzite BIF	Ijil Complex-Mhouidat Unit	3.58
CT07RIM46-1	GUELB_ER_RICHAT	21.10424	-11.38902	409.8	microgabbro	Mgd	3.38
CT07RIM28_3	FDERIK	22.95836	-12.05477	306.3	hematite-quartzite BIF	Ijil Complex-Mhouidat Unit	2.96
CT07RIM34-1	FDERIK	22.69385	-12.4786	667.3	platey hematite	Ijil Complex-Tazadit Fm	2.89
CT07RIM28_4	FDERIK	22.95836	-12.05477	306.3	quartz-rich BIF	Ijil Complex-Mhouidat Unit	2.56
CT07RIM26_1	FDERIK	22.92158	-12.01114	340.8	hematite-quartzite BIF	Ijil Complex-Mhouidat Unit	2.34
EA07RIM11	FDERIK	22.68821	-12.47642	399.8			2.08

Table 2. Magnetic susceptibility measurements from the Islamic Republic of Mauritania.—Continued

Sample No.	200K Sheet	Latitude	Longitude	Altitude (m)	Lithology	Unit name	Susceptibility X10^{-3} SI
CT07RIM28_6	FDERIK	22.95836	-12.05477	306.3	hematite IF	Ijil Complex-Mhouidat Unit	2
EA07RIM37	GUELB_ER_RICHAT	21.10092	-11.39693	409.2		Groupe díAssabet El Hassiane	2
EA07RIM05	ATAR	20.74346	-13.26721	224		Cortege d'Iguilid	1.82
CT07RIM35-1	FDERIK	22.6894	-12.52959	732	conglomeratic HIF	Ijil Complex-Seyala Fm	1.77
CT07RIM13_1	AKJOUJT	19.90884	-14.1986	242	quartz-malachite-azurite		1.76
EA07RIM51	MOUDJERIA	17.00866	-12.59595	118.9		Groupe de Gueneiba	1.6
CT07RIM28_7	FDERIK	22.95836	-12.05477	306.3	hematite IF	Ijil Complex-Mhouidat Unit	1.48
CT07RIM56_2	MBOUT	16.85787	-12.76078	55.3	Fe-silica-carbonate gossan	El Mseigguem Gp-Ouechkech Fm	1.31
CT07RIM36-5	FDERIK	22.69007	-12.47592	455.7	hematite IF	Ijil Complex-Tazadit Fm	1.18
DB07RIM17a	AKJOUJT	19.68005	-14.77687	0	quartzite		1.12
CT07RIM40-1	EL_MREITI	23.02432	-7.72324	306.1	microgabbro	Md	1.12
CT07RIM43-1	GUELB_ER_RICHAT	21.06972	-11.45833	436.2	carbonatite		1.1
EA07RIM04	ATAR	20.74426	-13.26719	222.2		Cortege d'Iguilid	1.08
CT07RIM09_01	AKJOUJT	19.64752	-14.14104		massive siderite	Akjoujt Fm.	1.04
EA07RIM52	MBOUT	16.98215	-12.63856	97.6		Nappe sableuse superficielle rÈcente	1
CT07RIM57-4	MBOUT	16.6761	-12.7034	44.4	conglomeratic hematite IF	El Ghabra Gp-Oued Erdi Fm	0.921
EA07RIM18	FDERIK	22.95815	-12.05485	311.6		Complexe d'Ijil	0.838
EA07RIM48	MBOUT	16.99109	-12.6944	102.1		Groupe de Gadel	0.7
EA07RIM35	GUELB_ER_RICHAT	21.05221	-11.44514	380.3		Groupe díAssabet El Hassiane	0.65
CT07RIM41-1	GUELB_ER_RICHAT	21.05177	-11.44527	379.7	carbonatite		0.628
CT07RIM50_1	MBOUT	16.88505	-12.66901	102.4	silicified chlorite schist or quartzite	Gadel Gp	0.511
CT07RIM08_02	AKJOUJT	19.61453	-14.17876		massive goethite/quartz veins		0.471

Table 2. Magnetic susceptibility measurements from the Islamic Republic of Mauritania.—Continued

Sample No.	200K Sheet	Latitude	Longitude	Altitude (m)	Lithology	Unit name	Susceptibility $X10^{-3}$ SI
EA07RIM42	MOUDJERIA	17.43191	-12.93225	93.9		CortËge de KelbÈ	0.45
CT07RIM56_1	MBOUT	16.85787	-12.76078	55.3	quartz veined gossan	El Mseigguem Gp-Ouechkech Fm	0.429
DB07RIM41a	FDERIK	22.94159	-12.04178	0	paragneiss		0.381
CT07RIM07_01	AKJOUJT	19.6411	-14.24593	244.7	botryoidal goethite		0.372
CT07RIM14_2	AKJOUJT	19.82401	-14.29395		greenschist	Akjoujt Fm.	0.359
CT07RIM19_1	ATAR	20.56713	-13.47811	165.4	pyroxenite	Amsaga Complex-AMIg	0.352
CT07RIM11_01	AKJOUJT	19.90842	-14.19315		greenschist	St. Barbe Fm.	0.347
DB07RIM01a		0	0	0	chloritic metasandstone	St. Barbe Fm.	0.342
EA07RIM01	ATAR	20.77458	-13.17767	212.8		Complexe díAmsaga	0.337
DB07RIM21a	ATAR	20.004038	-13.903794	0	granite	Amsaga Complex	0.331
CT07RIM58-4	MBOUT	16.27813	-12.57414	60.2	hematite IF	El Mseigguem Gp-Bathet Jmel Fm	0.326
DB07RIM08a	AKJOUJT	19.96006	-14.40163	0	hornblende diorite	Amsaga Complex-Amg	0.32
EA07RIM12	FDERIK	22.68426	-12.47692	436.5		Complexe d'Ijil	0.299
EA07RIM46	MBOUT	16.88579	-12.6694	94.2		Groupe de Gadel	0.28
CT07RIM04_01	AKJOUJT	19.83344	-14.46997	108.2	quartz-calcite-chalcocite-malachite veined grayschist	Irarchene el Hamra Fm	0.262
CT07RIM53_1	MBOUT	16.88887	-12.66903	98.8	malachite coated silicified gossan breccia	Gadel Gp	0.228
CT07RIM28_2	FDERIK	22.95836	-12.05477	306.3	qtz-carb-chl altered greenschist	Ijil Complex-Mhouidat Unit	0.222
CT07RIM12_1	AKJOUJT	19.90424	-14.19838	205.5	banded Fe-oxide/malachite		0.212
CT07RIM10_01	AKJOUJT	19.64872	-14.13991		metarhyolite?	St. Barbe Fm.	0.201
CT07RIM13_2	AKJOUJT	19.90848	-14.1982	250.5	basalt	St. Barbe Fm.	0.198
CT07RIM02_02	AKJOUJT	19.83974	-14.41061		massive siderite	Atomai Fm	0.185

Table 2. Magnetic susceptibility measurements from the Islamic Republic of Mauritania.—Continued

Sample No.	200K Sheet	Latitude	Longitude	Altitude (m)	Lithology	Unit name	Susceptibility $X10^{-3}$ SI
CT07RIM58-2	MBOUT	16.27813	-12.57414	60.2	quartz veined hematite and Mn oxides	El Mseigguem Gp-Bathet Jmel Fm	0.175
EA07RIM02	ATAR	20.77532	-13.17788	209.8		Complexe díAmsaga	0.175
DB07RIM53a	AIN_BEN_TILI	25.36297	-9.91157	0	metasandstone	Complexe du Ghallamane-GLsc	0.167
DB07RIM35a	FDERIK	22.68426	-12.47692	0	quartzite		0.148
EA07RIM31	AIN_BEN_TILI	25.36275	-9.91024	308.6		Complexe du Ghallamane	0.131
CT07RIM33-3	FDERIK	22.67806	-12.45953	487	altered muscovite schist	Ijil Complex-Tazadit Fm	0.124
CT07RIM52_1	MBOUT	16.88724	-12.6682	87.2	jaspilite	Gadel Gp	0.119
CT07RIM19_2	ATAR	20.56713	-13.47811	165.4	norite	Amsaga Complex-AMIg	0.116
GB07RIM70A	MBOUT	16.66663	-12.76711	52	quartzite		0.111
CT07RIM63-2	NEMA	16.43581	-7.11352		siltstone	Teniagouri Gp-Ould Yenje Fm.	0.098
DB07RIM29a	CHINGUETTI	20.4971	-12.87567	0	tuff		0.097
CT07RIM16_2	ATAR	20.12659	-13.80491	100.6	tillite		0.097
CT07RIM52_2	MBOUT	16.88724	-12.6682	87.2	talc schist breccia	Gadel Gp	0.096
CT07RIM50_2	MBOUT	16.88505	-12.66901	102.4	silicified chlorite schist or quartzite	Gadel Gp	0.095
EA07RIM32	BLEKHZAYMAT	24.4998	-7.42517	356.6		Groupe de Blekhzaymat	0.09
CT07RIM16_1	ATAR	20.12659	-13.80491	100.6	malachite-bearing amphibolite and quartz vein		0.082
CT07RIM57-3	MBOUT	16.6761	-12.7034	44.4	massive Fe oxide gossan	El Ghabra Gp-Oued Erdi Fm	0.078
CT07RIM02_01	AKJOUJT	19.83974	-14.41061		massive siderite	Atomai Fm	0.075
DB07RIM51a	GLEIBAT_TENEBDAR	24.7835	-10.45706	0	alkalai granite	Cortege de Gleibat Tenebdar	0.067
CT07RIM63-1	NEMA	16.43581	-7.11352		siltstone	Teniagouri Gp-Ould Yenje Fm.	0.067
DB07RIM73a	MBOUT	16.33721	-12.62448	0	metagraywacke	El Ghabra Gp-Ould Moilid Fm	0.065

Table 2. Magnetic susceptibility measurements from the Islamic Republic of Mauritania.—Continued

Sample No.	200K Sheet	Latitude	Longitude	Altitude (m)	Lithology	Unit name	Susceptibility $X10^{-3}$ SI
DB07RIM22b		0	0	0	granite		0.063
CT07RIM54-4	MBOUT	16.84516	-12.75505	75.4	barite-hematite schist	El Mseigguem Gp-Ouechkech Fm	0.056
DB07RIM05a	AKJOUJT	19.92377	-14.44736	0	leucotonalite	Arhgejit	0.055
DB07RIM30a	CHINGUETTI	20.71637	-12.73695	0	tillite	Jbeliat	0.055
DB07RIM57a	BLEKHZAYMAT	24.46592	-7.35997	0	sandstone/conglomerate	Blekhzaymat Gp-BZam3	0.055
CT07RIM54-7	MBOUT	16.84516	-12.75505	75.4	massive barite-fluorite	El Mseigguem Gp-Ouechkech Fm	0.049
CT07RIM14_1	AKJOUJT	19.82401	-14.29395		quartz-Fe oxide		0.046
DB07RIM12	AKJOUJT	19.71916	-14.54732	0	tillite		0.045
DB07RIM64a	MOUDJERIA	17.47236	-12.96754	0	granite	Cortege de Kelbe	0.042
CT07RIM54-8	MBOUT	16.84516	-12.75505	75.4	massive barite	El Mseigguem Gp-Ouechkech Fm	0.041
CT07RIM33-2	FDERIK				quartzite/muscovite schist	Ijil Complex-Tazadit Fm	0.039
CT07RIM17_1	ATAR	20.34112	-13.57404		foliated granite	Amsaga Complex	0.038
CT07RIM58-3	MBOUT	16.27813	-12.57414	60.2	chlorite schist	El Mseigguem Gp-Bathet Jmel Fm	0.038
DB07RIM55a	BLEKHZAYMAT	24.49981	-7.42639	0	sandstone/conglomerate	Blekhzaymat Gp-BZam2	0.036
DB07RIM29c	CHINGUETTI	20.4971	-12.87567	0	tillite		0.034
CT07RIM39-1	EL_MREITI	23.25249	-7.41895	308.9	siltstone	Azlaf Group-Sub-group 2	0.033
DB07RIM11a	AKJOUJT	19.7487	-14.5676	0	tillite		0.031
DB07RIM28a	CHINGUETTI	20.502785	-12.854843	0	sandstone	Nouatil Gp.	0.031
DB07RIM77a	SELIBABI	15.13696	-12.17747	0	tuffaceous sandstone	Teniagouri Gp-Tek	0.03
DB07RIM31	CHINGUETTI	20.717	-12.73111	0	sandstone	Assabet el Hassiane	0.028
CT07RIM41-2	GUELB_ER_RICHAT	21.05177	-11.44527	379.7	sandstone	Assabet El Hassiane Gp-Abiodh Sub-Gp	0.028
DB07RIM54a	OUED_EL_HAMRA	26.51881	-8.46481	0	metasandstone	Blekhzaymat Gp	0.027
CT07RIM27_1	FDERIK	22.92158	-12.01114	340.8	calcrete breccia	Ijil Complex	0.027
DB07RIM62a	ALEG	17.41983	-13.1377	0	metasandstone	El Fadra Gp-FrKc	0.026

Table 2. Magnetic susceptibility measurements from the Islamic Republic of Mauritania.—Continued

Sample No.	200K Sheet	Latitude	Longitude	Altitude (m)	Lithology	Unit name	Susceptibility $X10^{-3}$ SI
DB07RIM06a	AKJOUJT	19.94483	-14.40638	0	sandstone	Nouatil Gp.	0.025
DB07RIM74a	MBOUT	16.29167	-12.08789	0	sandstone	Oujeft Gp-Moudjeria Fm	0.025
EA07RIM40	MOUDJERIA	17.49395	-12.91461	95.5		Groupe de Gadel	0.025
DB07RIM77b	SELIBABI	15.13696	-12.17747	0	sandstone	Teniagouri Gp-Tek	0.023
DB07RIM76a	MBOUT	16.27028	-12.16705	0	graywacke	Djonaba Fm	0.022
DB07RIM80a		0	0	0	tillite	Jbeliat	0.021
CT07RIM06_01	AKJOUJT	19.64173	-14.25272	183.9	quartz breccia with malachite-chalcocite		0.021
CT07RIM54-6	MBOUT	16.84516	-12.75505	75.4	epidote altered felsic volcaniclastic	El Mseigguem Gp-Ouechkech Fm	0.02
EA07RIM58	MBOUT	16.29207	-12.08658	62.3		Groupe díOujeft	0.02
EA07RIM60	MBOUT	16.27077	-12.16557	83.6		Groupe de Djonaba	0.02
CT07RIM54-3	MBOUT	16.84516	-12.75505	75.4	epidote altered muscovite schist	El Mseigguem Gp-Ouechkech Fm	0.014
DB07RIM10a	AKJOUJT	19.79443	-14.48241	0	granite	Amsaga Complex	0.01
EA07RIM39	OUADANE	20.92858	-11.59211	399.8			0.01
CT07RIM57-2	MBOUT	16.6761	-12.7034	44.4	kyanite schist	El Ghabra Gp-Oued Erdi Fm	0.008
CT07RIM15_1	EL_GLEITAT	19.99854	-13.93906	102.8	cpy-malachite in quartz vein		0.007
EA07RIM14	FDERIK	22.60856	-12.42674	436.5		Groupe de Char	0.007
EA07RIM36	GUELB_ER_RICHAT	21.16336	-11.38809	400.4		Groupe díAssabet El Hassiane	0.007
EA07RIM38	GUELB_ER_RICHAT	21.08419	-11.40896	397.3		Groupe díAssabet El Hassiane	0.007
CT07RIM51_1	MBOUT	16.8859	-12.66704	81.5	silicified chlorite-sericite-carbonate schist	Gadel Gp	0.006
DB07RIM02a		0	0	0	quartzite	Ouamichoueima Gp-Atilis Fm	0.005
DB07RIM45a	FDERIK	22.69307	-12.4593	0	pegmatite		0.005

Table 2. Magnetic susceptibility measurements from the Islamic Republic of Mauritania.—Continued

Sample No.	200K Sheet	Latitude	Longitude	Altitude (m)	Lithology	Unit name	Susceptibility $X10^{-3}$ SI
CT07RIM23_1	ATAR	21.29333	-13.19777	236.8	garnet orthogneiss	Amsaga Complex-AMIg	0.005
DB07RIM66a	MBOUT	16.87144	-12.70554	0	quartz muscovite schist	Gadel Gp	0.003
DB07RIM11c					rhyolite		0.002
DB07RIM25a	ATAR	20.68434	-13.19708	0	granite	Amsaga Complex-Amg	0.002
DB07RIM26a	CHINGUETTI	20.004038	-12.83067	0		Chinguetti Fm	0.002
DB07RIM46a	FDERIK	22.67848	-12.46013	0	quartzite		0.002
DB07RIM52a	BEL_GUERDAN	25.15799	-10.12549	0	quartz arenite	Complexe de Tsalabia el Khadra-Khep	0.002
DB07RIM72a	MBOUT	16.48845	-12.65754	0	quartzite	Oua Oua Fm	0.002
CT07RIM28_1	FDERIK	22.95836	-12.05477	306.3	greenschist	Ijil Complex-Mhouidat Unit	0.002
EA07RIM30	AIN_BEN_TILI	25.35746	-9.91017	313.7		Complexe du Ghallamane	0.002
GB07RIM56C		17.43784	-12.92879	0	quartzite		0.001
GB07RIM63A	MOUDJERIA	17.08795	-12.9394	130	felsic tuff	El Ghabra Gp	0.001
GB07RIM80A	CHAMI	20.535261	-15.554685	88	quartzite		0.001
DB07RIM07	AKJOUJT	19.94646	-14.40501	0	sandstone	Nouatil Gp.	0.001
DB07RIM16a	AKJOUJT	19.71468	-14.56206	0	granodiorite	HDgn	0.001
DB07RIM23a	ATAR	20.29909	-13.17002	0	sandstone	Atar Gp-Foum Chor Fm	0.001
DB07RIM24a	ATAR	20.55003	-13.10027	0	sandstone	Atar Gp-Foum Chor Fm -Atf	0.001
DB07RIM25c	ATAR	20.68434	-13.19708	0	quartzite	Amsaga Complex-Amg	0.001
DB07RIM27a	CHINGUETTI	20.503337	-12.848143	0	sandstone	Nouatil Gp.	0.001
DB07RIM37a	FDERIK	22.60856	-12.42675	0	sandstone	Char Gp	0.001
DB07RIM58a	TIN_BESSAIS	23.04815	-8.18791	0	sandstone	Assabet el Hassiane-AhTb	0.001
DB07RIM59a	GUELB_ER_RICHAT	21.16323	-11.3894	0	sandstone	Assabet el Hassiane-AhTb	0.001
DB07RIM61a	OUADANE	20.92858	-11.5921	0		Chinguetti Fm	0.001
DB07RIM63a	MOUDJERIA	17.49605	-12.97836	0	quartzite	El Hneikat Fm	0.001
DB07RIM65a	MBOUT	16.88596	-12.72495	0	metaconglomerate	Gadel Gp	0.001
DB07RIM67a	MBOUT	16.88336	-12.66873	0	metasandstone	Gadel Gp	0.001
DB07RIM75a	KIFFA	16.34693	-11.97703	0	sandstone	Oujeft Gp-Oja Fm	0.001

Table 2. Magnetic susceptibility measurements from the Islamic Republic of Mauritania.—Continued

Sample No.	200K Sheet	Latitude	Longitude	Altitude (m)	Lithology	Unit name	Susceptibility $X10^{-3}$ SI
CT07RIM08_01	AKJOUJT	19.61453	-14.17876		silica-carbonate breccia	Irarchene el Hamra Fm	0.001
CT07RIM37-1	OUED_EL_HAMRA	26.33772	-8.53738	435.9	quartz-veined pyritic metatuff	Blekhzamat Group-Aguelt Nebkha Fm	0.001
CT07RIM44-1	GUELB_ER_RICHAT	21.10309	-11.39881	400.1	dolomite	Atar Gp-Tifounke Fm	0.001
CT07RIM44-2	GUELB_ER_RICHAT	21.10309	-11.39881	400.1	dolomite	Atar Gp-Tifounke Fm	0.001
CT07RIM45-1	GUELB_ER_RICHAT	21.10309	-11.39881	400.1	siliceous breccia	Atar Gp-Tifounke Fm	0.001
CT07RIM46-2	GUELB_ER_RICHAT	21.10424	-11.38902	409.8	silicified dolomite breccia	Atar Gp-Tifounke Fm	0.001
CT07RIM48-1	MOUDJERIA	17.43202	-12.93219	95.5	quartz veined quartzite	Gaoua Fm (?)	0.001
CT07RIM54-5	MBOUT	16.84516	-12.75505	75.4	felsic tuff	El Mseigguem Gp-Ouechkech Fm	0.001
CT07RIM57-1	MBOUT	16.6761	-12.7034	44.4	quartz -Fe oxide vein breccia	El Ghabra Gp-Oued Erdi Fm	0.001
CT07RIM58_1	MBOUT	16.27813	-12.57414	60.2	barite-Mn oxide	El Mseigguem Gp-Bathet Jmel Fm	0.001
EA07RIM59	KIFFA	16.34693	-11.97703	106.1		Groupe d'Oujeft	0.001

ISSN 2331-1258 (online)
http://dx.doi.org/10.3133/ofr20131280